AN EXPERIMENTAL STUDY OF FLUID-STRUCTURE INTERACTION IN COLLAPSIBLE VESSELS

A Thesis
Submitted to the Graduate Faculty
of the
North Dakota State University
of Agriculture and Applied Science

By

Jennifer Ida Alexandra Schmeling

In Partial Fulfillment of the Requirements
for the Degree of
MASTER OF SCIENCE

Major Department:
Mechanical Engineering

June 2022

Fargo, North Dakota

North Dakota State University
Graduate School

Title

AN EXPERIMENTAL STUDY OF FLUID-STRUCTURE INTERACTION IN COLLAPSIBLE VESSELS

By

Jennifer Ida Alexandra Schmeling

The Supervisory Committee certifies that this ***disquisition*** complies with North Dakota State University's regulations and meets the accepted standards for the degree of

MASTER OF SCIENCE

SUPERVISORY COMMITTEE:

Dr. Yan Zhang
Chair

Dr. Jordi Estevadeordal

Dr. Yao Yu

Approved:

06/29/2022
Date

Dr. Alan Kallmeyer
Department Chair

ABSTRACT

The fluid-structure interaction in collapsible thin-walled vessels is an important topic of research to better understand the physical mechanisms behind many physiological processes and diseases. In this work, we established an experimental setup to study the collapsible tube deformation and fluid-structure interaction within a thin-walled collapsible vessel. The effects of transmural pressure and flow rate were characterized experimentally using high-frequency pressure transducers and optical measurements. Various transmural pressures were also simulated through finite element analysis. Results suggest that the deformation of thin-wall vessel follows the pattern described by Shapiro's tube law. The collapsed pattern and cross-sectional area changes with different transmural pressure and flow pressure gradients. Below a certain negative transmural pressure threshold, we observed self-induced oscillations whose frequency and magnitude are functions of flow rates. The critical non-dimensional parameter thresholds for self-induced oscillation and the related fluid flow behaviors were examined using Particle Image Velocimetry.

ACKNOWLEDGMENTS

I'd like to gratefully acknowledge my advisor Dr. Yan Zhang for his guidance, continued support, and knowledge passed on throughout the duration of my graduate studies.

I would also like to thank the rest of my committee members, Dr. Jordi Estevadeordal and Dr. Yao Yu, for their time, constructive comments, suggestions, and critiques.

Lastly, I would like to thank my family and friends who have had my back and been better cheerleaders than I could have ever asked for. I wouldn't be where I am today without them.

TABLE OF CONTENTS

LIST OF TABLES

LIST OF FIGURES

LIST OF ABBREVIATIONS

LU	Low frequency oscillations where most of the oscillation cycle is spent with its downstream pressure greater than the midpoint between the two pressure extremes.
LD	Low frequency oscillations where at least half of its oscillation cycle is spent with its downstream pressure less than the midpoint between the two pressure extremes.
FEA	Finite element analysis.
PIV	Particle image velocimetry.
FFT	Fast Fourier transform.

LIST OF SYMBOLS

p ..... Internal pressure

p_e ..... External pressure

$\tilde{P}(A)$ ..... Representation of tube law

A ..... Cross-sectional area

A_0 ..... Neutral cross-sectional area

Re ..... Reynolds number

σ_0 ..... Dimensionless prestress

α ..... Womersley number and normalized cross-sectional area

P_1 ..... Pressure upstream of collapsible tube

Q_1 ..... Flow rate upstream of collapsible tube

P_2 ..... Pressure downstream of the collapsible tube

Q_2 ..... Flow rate downstream of the collapsible tube

P_u ..... Total upstream pressure

R_1 ..... Rigid pipe upstream of collapsible tube

R_2 ..... Rigid pipe downstream of collapsible tube

Q ..... Flow rate

ρ ..... Fluid density

u ..... Longitudinal fluid velocity

t ..... Time

x ..... Longitudinal distance

D ..... Wall distensibility

c ..... Wave speed

S ..... Speed index and Type A durometer hardness

E	Elastic/Young's modulus
C	Transformation matrix
Π	Normalized transmural pressure
K_p	Flexural rigidity
ν	Poisson's ratio
γ	Ratio of tube's wall thickness to the internal radius
Δp	Pressure difference across the collapsible tube
$P(x,y,z)$	Pressure equation for finite element analysis
$F(x,y,z)$	Equation of pressure gradient for finite element analysis
a	Coefficient of pressure gradient in x-direction for finite element analysis

LIST OF APPENDIX FIGURES

1. INTRODUCTION

1.1. Background

Vessels within the body are plentiful and used to circulate a variety of fluids including air and blood throughout the respiratory and circulatory systems. In an average adult, these vessels can range in diameter from five to ten microns on the smaller end of the spectrum with capillaries to two or three centimeters in arteries and veins [1]. Circumstances – such as vessel size and vessel location within the body – can dictate whether the fluid flow within vessels is steady or pulsatile. For blood flow specifically, pulsatile flow tends to be due to the pulsatile nature of the heart and therefore is found in regions close to the heart and in large arteries. Some vessels – particularly large veins – have the tendency of collapsing under a specific set of conditions. This collapsed vessel leads to a reduced or completely stopped flow. The two factors that can combine to create a collapsed vessel are the vessel's wall thickness and the transmural pressure.

Vessels like veins, not arteries, tend to have thin walls that lend to a propensity to collapse under a negative transmural pressure. Transmural pressure is defined as the pressure difference between outside and inside of a vessel. A negative transmural pressure means a higher pressure is present outside the vessel when compared to the internal pressure. The greater external pressure on the vessel with thin walls tends to lead to collapse of varying degree depending on how negative the transmural pressure becomes. The collapse of vessels due to wall thickness and transmural pressure is caused by the relationship between the transmural pressure and the cross-sectional area of the vessel known as the local tube law. Mathematically, the local tube law is generally presented in the form popularized by Ascher H. Shapiro in 1977 as

$$p - p_e = \tilde{P}(A) \tag{1}$$

where $\tilde{P}(A)$ represents the tube law shown in Figure 1, p is the internal pressure within the tube, and p_e is the external pressure [2]. Combining the local tube law with the effects of pulsatile blood flow conditions near the heart, the transient fluid-structure interaction of blood flow within collapsible vessels becomes complicated for computational studies.

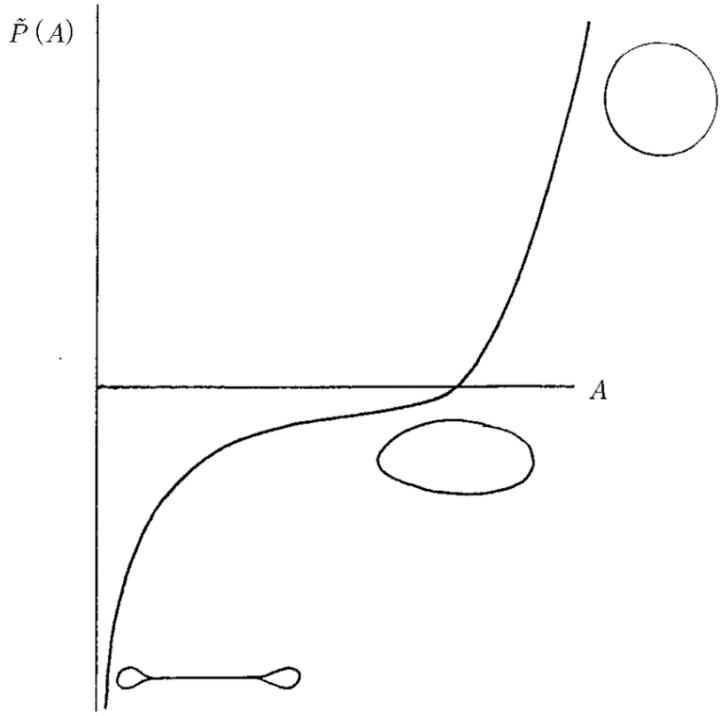

Figure 1. Tube law shown as the relationship between transmural pressure ($\tilde{P}(A)$) and the cross-sectional area (A) [3].

Historically, experimental studies pertaining to the blood flow within a body have proven difficult to complete. Due to this, many such experiments take place in vitro, or outside of the body. In place of human blood vessels, substitutes are often used in the in vitro experiments. Obvious replacement choices include other biological blood vessels, such as veins from cows, giraffes, or dogs [4], [5]. Synthetic alternatives, such as rubber or silicone tubing, is also available. One common synthetic alternative to the blood vessel and its surroundings is to use a "Starling resistor." The Starling resistor was invented in 1912 by British physiologist Ernest Starling. Starling primarily focused on bodily functions and contributed to modern understanding

of several functions including mechanical controls of heart function and the balance of fluids through tissue [6]. Starling resistors consist of a pressurized chamber that connects to a steady or pulsatile flow loop. The collapsible tubing segment runs along the inside of the pressurized chamber and is the link between the chamber and the flow loop. Rigid tubing segments support the collapsible tubing and connect it to the outside flow loop. A typical schematic of a Starling resistor can be seen in Figure 2.

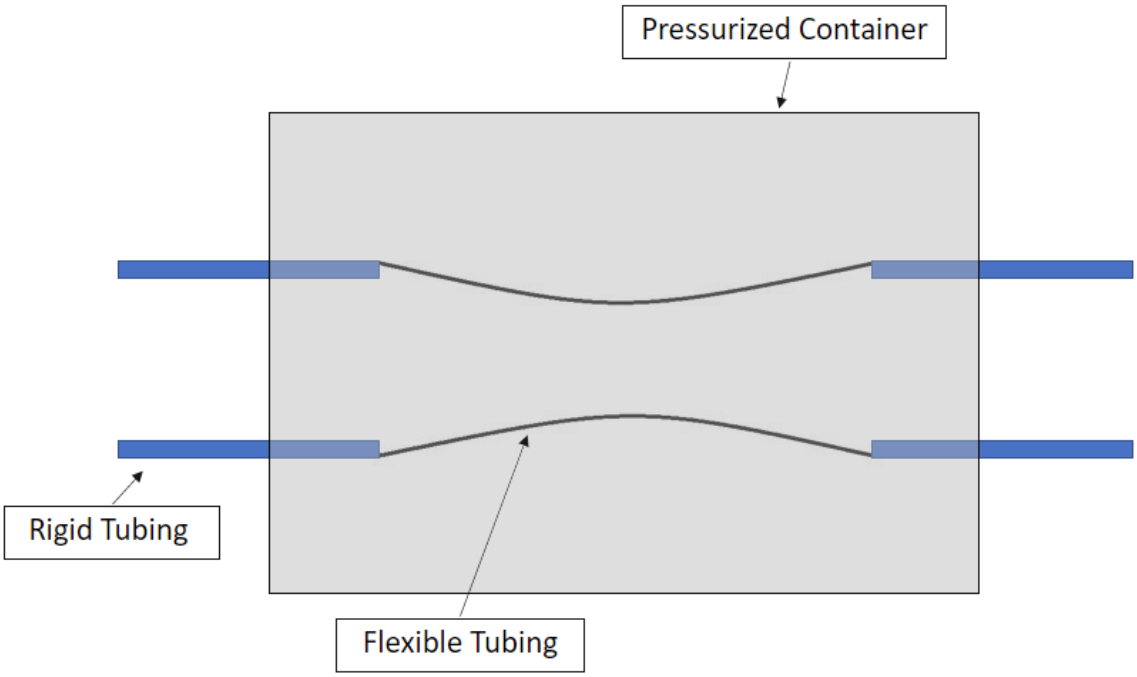

Figure 2. Diagram of a Starling resistor.

Pressurizing the container allows for control over the flow through the collapsible tube through the degree of collapse the tube experiences. Starling initially used this device to simulate flow between the heart and lungs to control blood pressure [7]. While it was originally invented with the primary intention of understanding the functions of the heart, Starling resistors are now thought of as potential models for multiple flow types. They are commonly used as the experimental model for exploring the effects of pressure and flow on the oscillations and cross-

sections of vessels. The Starling resistor is not limited to liquids as the working fluid; air and other gasses can be used as the working fluid for experimental research. This allows the Starling resistor to be used to simulate vessels in the lungs in addition to blood vessels, though using water as the working fluid means the fluid density and tube wall density ratio is incorrect for the lung by a factor of 103, disallowing many comparisons for these types of work with those completed using air as the working fluid [8].

Collapsible vessels are found in multiple physiological processes within the body and can be involved in a number of health conditions and impairments. One condition related to vessel collapse is the lumen collapse of tubular structures. A lumen, or the cavity or channel within a tube such as a vein or intestine, can be simulated using a Starling resistor [9]. The existence of stenosis within a vessel can also be compared to its collapse, given the limitations to flow that occur [10]. Circulatory failure is a broad term given to any condition where the pressure inside of the vessel, generally the arterial pressure, and the flow within the vessel are reduced to an extent that organ function is impaired and the damaged organ function cannot be returned to normal activity levels [11].

Vessel collapse does not always indicate an impairment of health within the body. Healthy veins regularly collapse due to changes in the body's position, such as shifting from a supine position to standing upright. Vessel collapse can also be stimulated by external forces. Pneumatic pressure cuffs collapse arteries of extremities in order to prevent hemorrhage during surgery [12]. Doctors, nurses, and other medical staff regularly use an instrument called a sphygmomanometer to measure blood pressure; the cuff is wrapped around the patient's upper arm and inflated to stop blood flow in the artery through collapsing the vessel [13].

1.2. Literature Review

Historically, interest in collapsible vessels is well documented. Studies have been done using theoretical methods, experimental methods, or a combination of the two. These studies generally tend to use the Starling resistor model as a substitute for human blood or fluid vessels. The first use of the Starling resistor, as previously mentioned, was by Starling and F. P. Knowlton in 1912 in a study of the impact of temperature and blood pressure variations on isolated mammalian heart performance [14]. Pioneering studies with collapsible tubes have found that veins play a large role in controlling the output of the heart; this controlling function was found to be passive and the result of the veins' ability to inflate and collapse [15].

1.2.1. Theoretical Studies

Theoretical studies generally consist of a mathematical or numerical solution to the presented problem. These types of studies are done to reduce the number of experimental studies that need to be done and generally use experimental data to confirm the accuracy and validity of the theoretical model. A mathematical model of varying degree is created based on a real-world scenario; the scenario is then simulated using a number of algorithms. Pedley and Luo (1997) presented a review of model types for analyzing flow and oscillations in collapsible tubes. Zero-dimensional models are the earliest model type; these are functions only of time. Lumped parameter models are in-between zero- and one-dimensional models in terms of complexity; the modelled system is more detailed than a zero-dimensional model, but components are "lumped" together in a semblance of a black box scenario to simplify the system [3]. Hayashi et al. (1994) derived a lumped parameter model of steady flow in collapsible tubes to describe dynamic flow behavior, investigate the flow stability, and clarify the tube's self-excited oscillation mechanism. The study found that statical instability was due to load resistance while dynamic instability was

due to load inertance. They also found that self-excited vibrations occurred with negative resistance exceeding load resistance. The theoretical instabilities agreed with comparable experimental results [16]. A Starling-like resistor lumped parameter model was developed to look at flow through a semi-collapsed vessel when the transmural pressure was negative. The model was consistent with other computational and experimental models where the tube was capable of withstanding nominal negative transmural pressures before collapsing [17].

One-dimensional models increase the level of complexity by taking the tube's cross-sectional area, internal pressure, and average fluid velocity as functions of the longitudinal coordinate and time. A modified, composite one-dimensional, time independent numerical model – which can be known as a quasi-one-dimensional model – was presented in 2005 with a new feature that related the skin friction coefficient to the Reynolds number for a particular flow rate. The model was used to show the typical variation in area, velocity, and pressure along the tube within a Starline resistor in a collapsed state, shown in Figure 3. A is the cross-sectional area of the collapsible tube and A_0 is the neutral cross-sectional area prior to any deflection. More complicated models have shown that the smallest cross-sectional area after tube collapse tends toward the outlet of the tube, as opposed to closer to the middle as shown here. The model predicted phenomena that had been previously discussed in literature as well as provided a way to study the effect of longitudinal wall tension on the collapsible tube system [18].

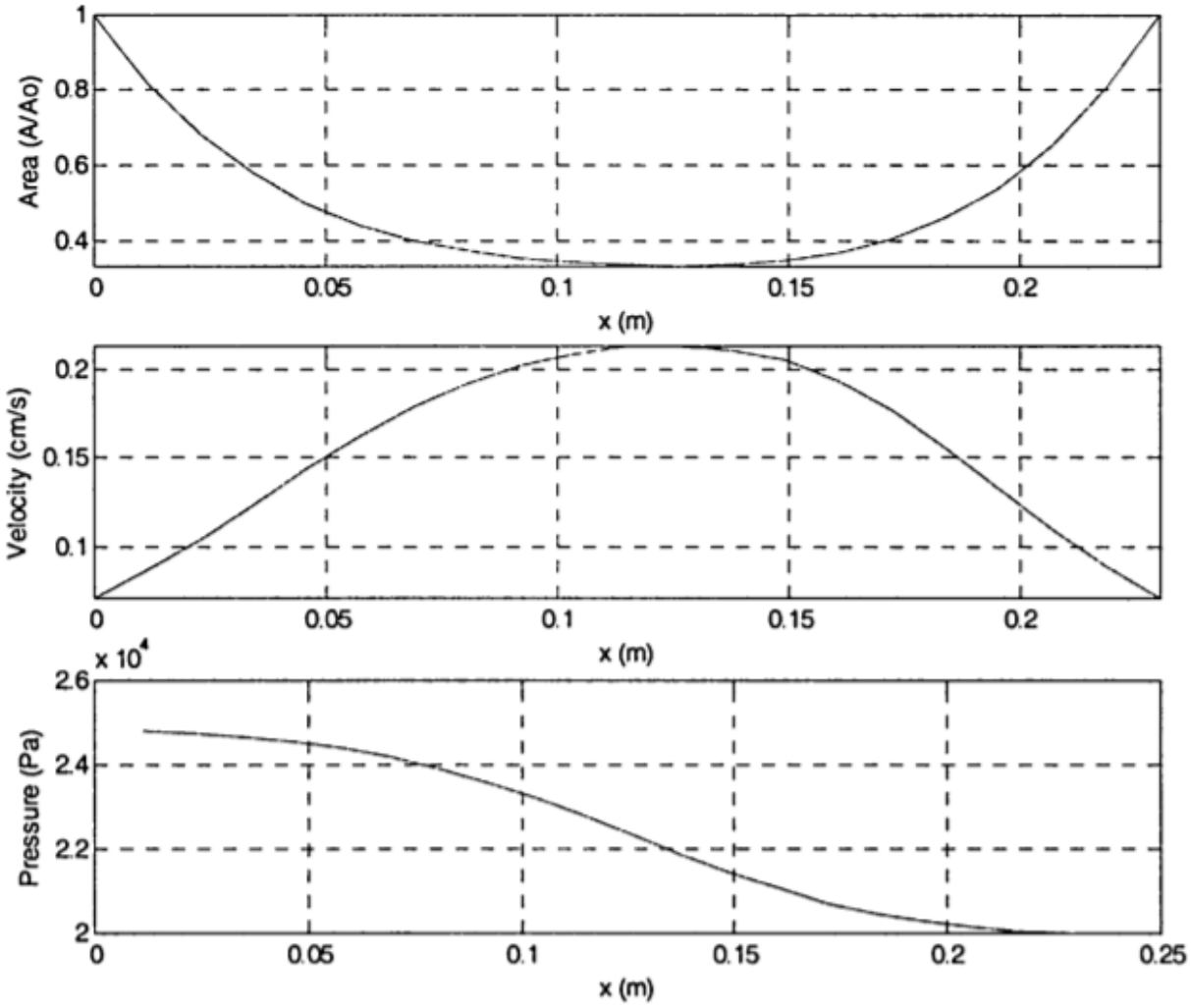

Figure 3. Graphs showing the variation in area, velocity, and internal pressure along a collapsed tube [18].

Two-dimensional models were generally used for studying unsteady and steady flows and the mechanisms of instability and oscillations of the flow. Figure 4 shows the streamline plots at several different times during self-excited oscillations at a specified Reynolds number of a two-dimensional model. It highlights the flow separation that may exist after tube wall collapse in a quasi-steady flow but may not exist in an unsteady flow [3].

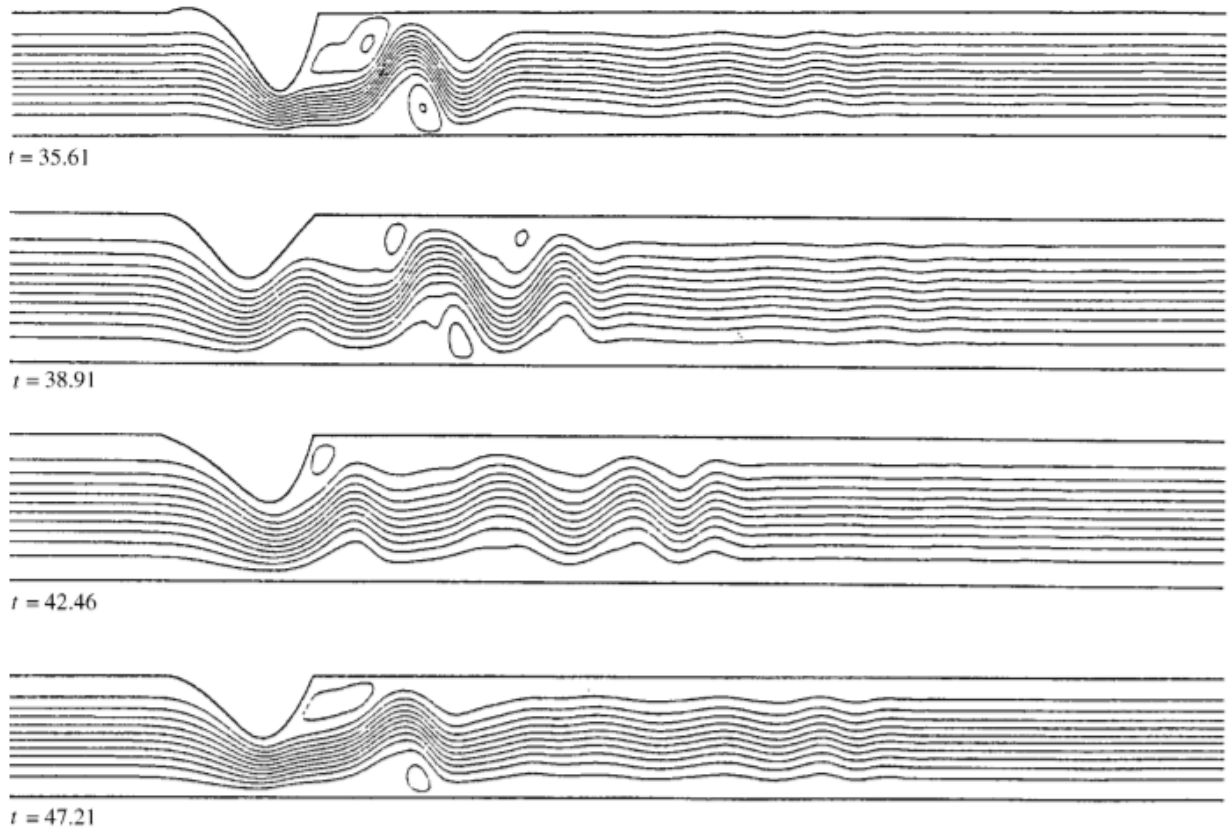

Figure 4. Streamline plots at four different times during self-excited oscillations at Re=300 [3].

Jensen and Pedley looked at steady flow in collapsible tubes and presented a set of equations and the solution for a steady state system. For a flow of dimensionless length that is fully attached, two solutions exist with a totally collapsed tube. For separated flow, one fully collapsed solution was found with no choking phenomena [19]. Luo and Pedley provided a completed description of steady and unsteady flow in a two-dimensional collapsible channel that included self-excited oscillations. The study found that while the deflection of the wall initially increased as the tension was reduced, different Reynolds numbers influenced the continued wall deflection. With a Reynolds number of one, the tension reduction continued until a critical value was reached, after which no converged solution occurs. With Reynolds numbers of 100 and 500, the maximum wall deflection happened at longitudinal tension values that were dependent on other variables. The study concluded that more complete computations of unsteady flow and

three-dimensional flows are needed before the mechanism behind self-excited oscillations can be understood [20].

Xu et al. studied the interactions between elastic structures and flow-induced pressure oscillations in order to look at the resonances in pulsatile flow with elastic walls. The study used a mathematical model of the system to describe the response of a collapsible tube using a harmonic oscillator with non-standard damping – including in regions with large wall deflections caused by fluid pressure oscillations, providing another way to look at the problem of the collapsible tube. Pressure contours and streamlines at four equally spaced points within one period of oscillation after the decay of initial transients is shown in Figure 5; case (a) shows the collapse of the elastic tubing while case (c) shows an expansion of the elastic tubing due to oscillations. Both (a) and (c) displace a significant amount of fluid from the central area of the tubing which causes a sloshing flow that feeds back into the pulsatile flow [21].

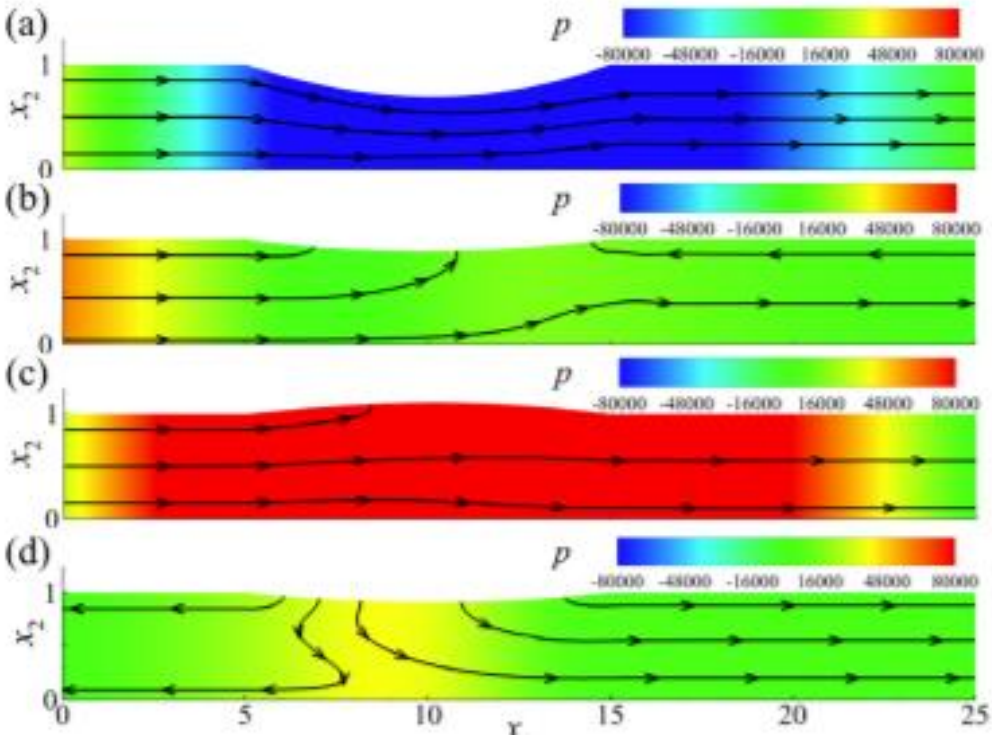

Figure 5. Pressure contours and streamlines at equally spaced snapshots through a period of oscillation for Re=100, σ_0=dimensionless prestress=10^3, p_{ext}=10^{-4}, and α^2=squared Womersley number=148 [21].

A Starling resistor was used to develop a model of the power-law fluid flow past a flexible tube in order to investigate global static stability of a prestressed axisymmetric collapsible elastic tube with a non-Newtonian fluid. Within the Starling resistor, the global stability was largely influenced by the physical nonlinearity of the fluid. The static instability was associated with non-uniqueness of the solution to the boundary value problem [22]. A modified Starling resistor was used to investigate oscillations in blood vessels. It was found that self-excited oscillation of the deformable tube portion might be triggered by the externally applied pressure, where higher pressure applied meant stronger oscillations. This model also verified the general belief that the lowest point of the wall during oscillation tends towards the end portion of the collapsible tube [23]. A theoretical Starling resistor with a pressure-driven flow was proposed in 2017; the flow and the transmural pressure were generated from the same

source. This was a novel approach that allowed users to choose inlet resistance and the design of the flexible tubing in order to get the desired flow rate and activation pressure for collapse. The study found that inner tube diameter was a determining factor to the limitation mode of the resistor. It was also determined that the tube length was able to increase the time-averaged flow rate in the oscillation regime of the flow limitation range but not during the steady state. Also discussed were two types of oscillation, shown in Figure 6, where type (a) starts from fully open tubing and type (b) starts from an already reduced cross-sectional area [24]. A study using a thin-walled tube in the Starling resistor found that the cross-section of the tube changed from circular to elliptical to a dumbbell shape with increased pressure within the Starling resistor chamber under no flow conditions [25].

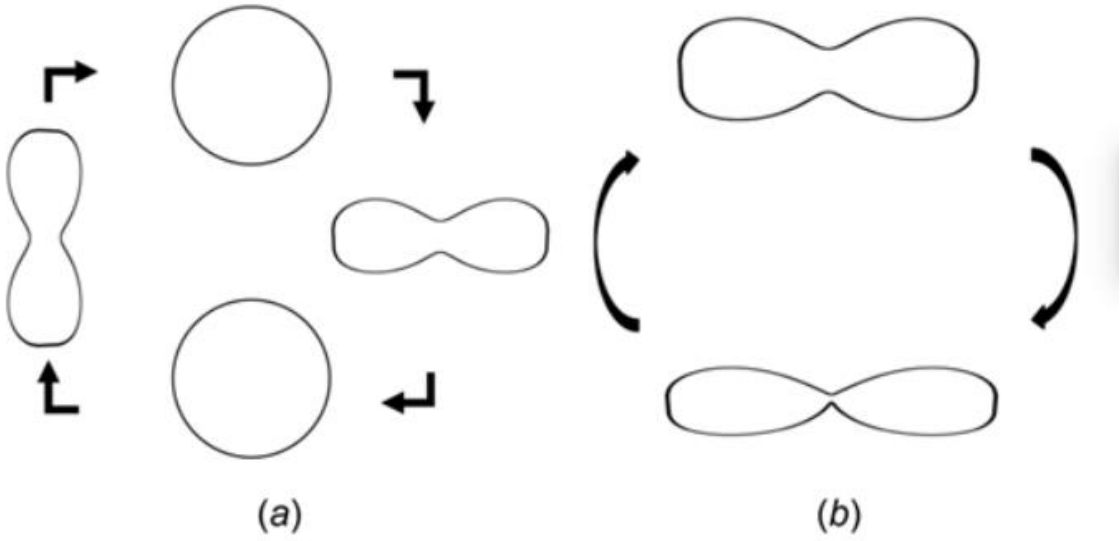

Figure 6. Two types of oscillations. Type (a) is where the tube walls oscillate between two non-axisymmetric extremes and type (b) is where the wall has small-amplitude oscillations around one of the non-axisymmetric extremes [24].

Additional oscillation types have been known to occur when using a Starling resistor, generally dependent on factors such as classifying the tube as thin- or thick-walled. Thick-walled tubes tend to display two oscillation modes known as “milking” oscillation and stationary

oscillation. Milking oscillations are large-amplitude lower-frequency wall oscillations that move down the length of the tube, partially or completely interrupting the flow. Stationary oscillations tend to be higher-frequency oscillations that have a stationary choke point that have little to no effect on the flow [26]. Thin-walled tubes tend to have many types of LU and LD mode oscillations that are differentiated based on the number of tube collapses within one complete cycle. LU mode is a class of low frequency oscillations where the tube is open for most of the oscillation cycle and most of the cycle is spent with its downstream pressure above the midpoint between the two downstream pressure extremes; LD mode is a class of low frequency oscillations where the tube is not open for most of the oscillation cycle and at least half of its oscillation cycle is spent below the midpoint of the two downstream pressure extremes [25], [27].

Heil and Waters presented a computational and theoretical analysis of three-dimensional unsteady finite-Reynolds-number flows in collapsible tubes with walls that have prescribed high-frequency oscillations like the ones found in Starling resistor experiments. The model showed that in an experiment with fixed frequency oscillation, self-excited oscillations were likely to develop when the mean fluid flow exceeded a certain threshold of the inverse Strouhal number [28]. The Starling resistor and its behaviors have been added to the end of veins in models. The innate changes that deploying a Starling resistor allows to the system can be used to explore phenomenon that exist in areas such as the terminal part of cerebral veins that may not be able to be modelled more accurately another way [29]. Progress has been made in utilizing three-dimensional models. However, due to high computing costs and model complexity, two-dimensional models continue to be the predominant model to use in investigating the dynamic behavior of the collapsible veins [23].

1.2.2. Experimental Studies

A multitude of studies also investigated phenomena using an experimental Starling resistor. Figure 7 shows a simple laboratory experimental setup. The collapsible tube, an integral part of the Starling resistor model, must be a tube with flexible enough walls to allow for deformation to a highly non-circular cross-sectional area when the transmural pressure is negative [15].

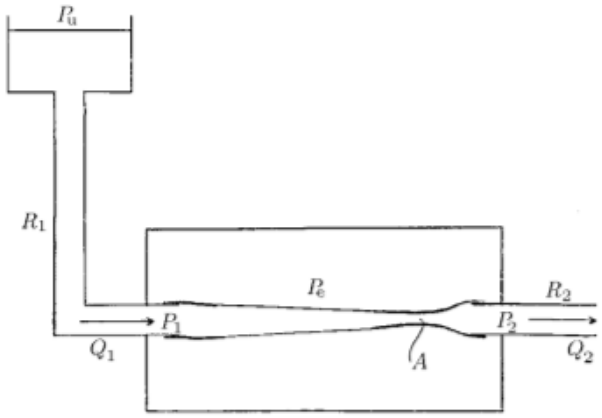

Figure 7. Sketch of standard laboratory where P_1 and Q_1 are the pressure and flow rate upstream of the collapsible tube, P_2 and Q_2 are the pressure and flow rate downstream, P_u is the total pressure upstream, P_e is the external pressure within the chamber, and R_1 and R_2 are the rigid pipes on either side of the collapsible tube [3].

Conrad examined the pressure-flow relationship in collapsible tubes. It was shown that as the external pressure increased, the initial resistance of the tube walls increased proportionally but the final resistance remained unchanged. It was also shown that there were three geometry-based flow states for the collapsible tube [30]. Kececioglu et al. studied steady, supercritical flows in thin-walled compliant tubes in order to determine characteristics of supercritical flows. The Starling resistor model was used to examine the local tube law and geometry of the collapsible tube at various pressures due to partially collapsed veins having a higher likelihood of achieving supercritical flow [31]. Stelios et al. examined the behaviors and differences of

collapsible tubes mimicking blood vessels with differing wall thicknesses [32]. Figure 8 shows the relationship between the transmural pressure and the cross-sectional area once tube buckling began.

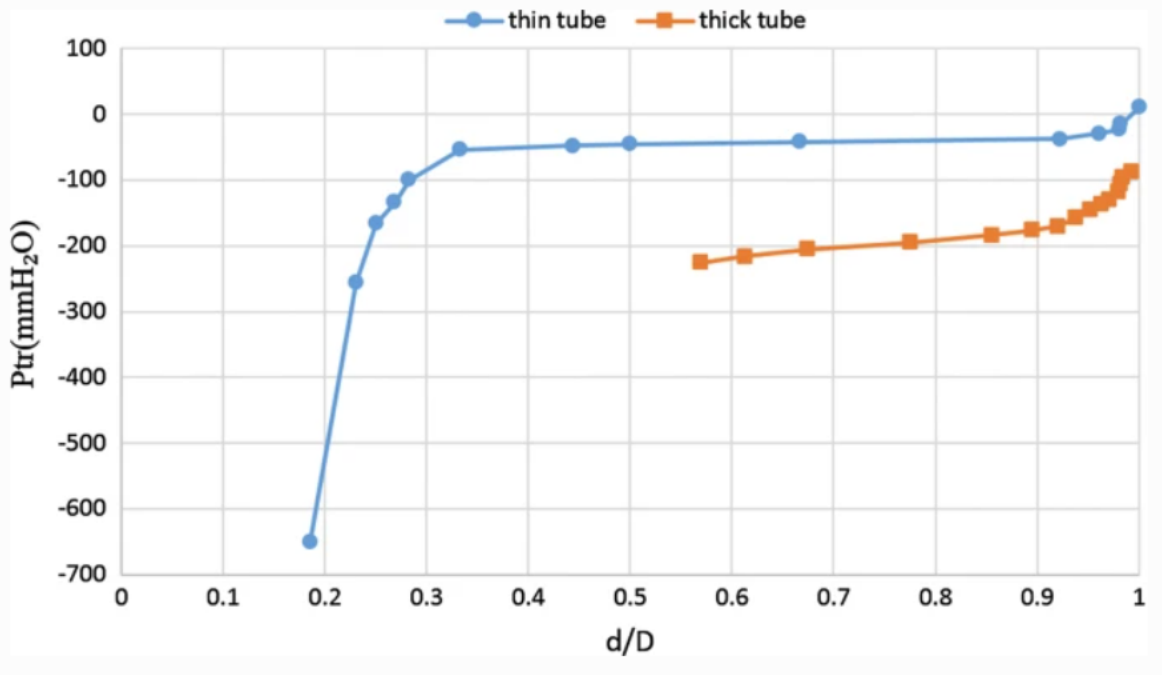

Figure 8. Transmural pressure vs. smallest distance between opposite tube walls for thin- and thick-walled tubes [32].

The slope of the thin tube is slightly smaller than the slope of the thick tube, but both resulted in small wave speed. This can lead to flow instabilities if the fluid velocity exceeds the wave speed. Two pumps were used to simulate forced and unforced flow. Larger tube oscillations occurred when a peristaltic pump was used when compared to the progressive cavity pump; when the transmural pressure became negative, the self-excited oscillations started within the tube, causing the cross-section to become two-lobed and elliptic [32]. Nahar et al. examined the flow of both Newtonian and non-Newtonian fluids under a range of transmural pressures. The conclusion was reached that the tube's deformation depends on the applied pressure as well as the tube's modulus and the type of working fluid [33]. A Starling resistor model with a

"floppy tube" in the place of the collapsible tube portion of the model was used to demonstrate the complicated interaction between longitudinal wall strain and the surrounding pressure. With any strain, increasing the surrounding pressure led to decreased tube cross-sectional area, decreased airflow, and increased pressure difference between upstream and downstream flow in the model [34].

Studies into the sagittal sinus and cerebral veins and their corresponding pressures led to questions about whether a Starling resistor effect or waterfall effect exists between the two [5]. The existence of a pressure gradient when a catheter in the cerebral vein is moved from the subdural space into the sagittal sinus was confirmed. It was found that flow through lateral lacunae decreased as intracranial pressure increased though the flow never stopped completely despite the intracranial pressure. This can be explained in terms of an "intracranial venous pressure regulation mechanism" that can be modelled like a Starling resistor vascular waterfall model [5]. Air is an acceptable working fluid for a Starling resistor model, but it is expected to have distinctly different results when compared to a system that uses water as a working fluid [35].

A need was recognized for experimental data sets that were sufficiently characterized to validate three-dimensional models as well as be in a parameter range that agreed with modern numerical methods and computers. An experimental setup with the lowest possible Reynolds number for the experiment to be numerically simulated and a Starling resistor configuration that allowed the tube to collapse with and without oscillations. Figure 9 shows the onset and decay of oscillation in flows where the flow rate (Q) becomes essentially independent of the downstream pressure (p_2) as p_2 is reduced and the tube is in the process of collapsing. The experimental data collected was able to be used in order to determine the minimum Reynolds number for self-

excited oscillations to begin; it was also used to confirm older findings on flow rate limitations [36].

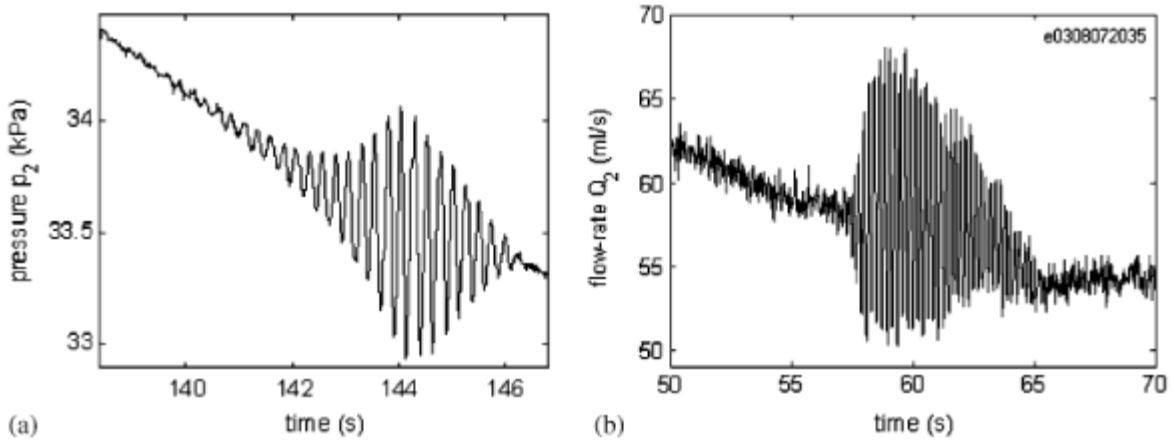

Figure 9. Oscillation burst. In (a) the burst is manifested from p_2 and in (b) it is manifested from Q_2 [36].

1.2.3. Combined Experimental and Theoretical Research

Many studies are not limited to being either theoretical or experimental, but instead combine the two approaches. Lambert and Wilson presented a model that addressed flow limitations in collapsible tubes and compared the results obtained to observed Starling resistor flows. It was determined that the model proposed was useful for describing the flow in a collapsible tube if the Reynolds number is large and the tube is not completely collapsed [37]. Heil and Hazel reviewed theoretical and experimental studies on fluid-structure interactions in flow through collapsible tubes. Expectedly, it was found that idealized models are the most common type employed and, while vessels within the body vary greatly in complexity when compared to a Starling resistor, Starling resistors have proven to be good approximations of blood vessels [38]. Kozlovsky et al. examined the tube law for thin- and thick-walled tubes to determine the role of wall thickness with post-buckling behavior [39]. Similar to [32], it was found that as negative transmural pressure exceeded the buckling pressure, the cross-section of

the tube decreased. Initially the tube deformed to an elliptic shape before progressing to a two-lobed shape and then completely flattening with opposite tube walls touching. All of the tubes buckled at the same transmural pressure, regardless of wall thickness [32], [39]. The knowledge of where the Starling resistor can be applied within the body is ever growing and changing. It was long thought that Starling resistor models were ideal for embolic pulmonary hypertension. With that model of pulmonary circulation, increased pressure intercept causes a vascular closing pressure that can become higher than left atrial pressure. However, more studies of this phenomenon showed that, experimentally, a distensible vessel model has a better agreement between measured and predicted pressures and flows [40]. Starling resistor pressure-flow relations can tend to be similar to other models as well, including the waterfall model. Investigations have looked at whether, at low Reynolds numbers, these relations tend toward the waterfall model meaning the second model would be applicable as well in some instances. It was concluded that the waterfall model is valid for exceedingly small blood vessels and that, experimentally, pressure-flow relationships are distinctly different at low and high Reynolds numbers [12].

While investigating obstructive sleep apnea differences in males and females, a Starling resistor was considered as a pharynx when the upper airway collapse was under scrutiny. Using finite element analysis, buckling of the tube was quantified to determine the effect of tube length on critical buckling pressure. Using the proposed model and comparing the results to experimental data collected, it was determined that shorter collapsible tubes can resist greater transmural pressures before buckling than their longer counterparts [41].

Based on the review of published literature available pertaining to the flow through collapsible tubes and Starling resistors, systematic experimental research in terms of both steady

and pulsatile flow in three-dimensional collapsible vessels is lacking. Previous theoretical research generally did not consider the pulsatile flow conditions and complex unsteady conditions, which are of particular interest in physiological flow phenomena. Future experimental studies using high-speed imaging and particle image velocimetry can significantly contribute to the knowledge of the fluid-structure interaction in unsteady flow through collapsible tubes.

1.3. Objective

In my thesis research, I proposed to study the fluid-structure interaction of a collapsible blood vessel (large vein) – including cross-section variations and self-excited oscillations – experimentally and numerically during steady blood-mimicking flow using a Starling resistor. An in vitro flow loop was used for particle image velocimetry and high-speed image measurements. A computer simulated mathematical model of flow through a collapsible blood vessel was also completed using the same flow characteristics. The specific objectives were:

- To understand the effects of external and internal pressure changes on the internal flow and cross-sectional area of the flexible tubing in the Starling resistor using *in vitro* steady experiments.
- To compare experimental results with computer simulated mathematical model of flow through a collapsible blood vessel.

The study was innovative because there is currently limited experimental research regarding the fluid-structure interaction of thin-walled vessels under unsteady flow conditions. The results of the thesis research will contribute to the knowledge of vein hemodynamics as well as provide insights to the prevalent vein diseases such as vein thrombosis.

The organization of the thesis can be summarized as follows:

Chapter 1: The background, literature review, and objective of the thesis was summarized.

Chapter 2: The research methods utilized were explained and the local tube law was validated.

Chapter 3: Steady flow was applied to the Starling resistor and the impact of Reynolds number and transmural pressure on the degree and location of collapse was explored.

Chapter 4: Steady flow was applied to the Starling resistor with the intent of determining the critical Reynolds numbers and transmural pressures necessary to trigger and terminate self-excited oscillations for the local collapsible tube.

The thesis will conclude with a section on future work, areas of improvement, limitations, and a summary of conclusions to be expanded on and discussed.

2. RESEARCH METHOD AND VALIDATION

2.1. Research Method

In this study, we utilized multiple methods of examining the effects of internal and external pressure changes on the internal flow and structural changes of the flexible tubing, including *in vitro* experiments and numerical simulations. The experimental and numerical simulations used the same range of values for flow rates and pressures. According to the literature survey, the biological flow rates within blood vessels ranged from 1.2 mL/min in small veins to 5 L/min at the normal cardiac output of adult humans [42], [43]. Reynolds numbers for blood flow within the body typically range from 1 in the smallest blood vessels such as small arterioles to upwards of 4,000 in larger arteries such as the aorta [44]. However, within small venules, Reynolds numbers as small as 0.01 have been estimated [45]. Within dogs, the average Reynolds numbers within veins is between 250 and 500, with a peak at 700; these values are smaller than anticipated with humans, but still provide an estimate range [46]. The largest Reynolds number is found in the vein closest to the heart – the vena cava. For midsized mammals such as dogs, the maximum Reynolds number was estimated to be 1,000; for humans a critical value of 2,000 is not expected to be exceeded under resting conditions [47]. Transmural pressures ranged from -50 mmHg to 50 mmHg and the internal pressure within the vessels ranged from 5 mmHg to 150 mmHg [48, p. 1], [49], [50].

2.1.1. Governing Equations

The governing equations for the quasi-one-dimensional system include the equation of motion

$$\frac{\partial u}{\partial t} + u\frac{\partial u}{\partial x} = -\frac{1}{\rho}\frac{\partial p}{\partial x} \tag{2}$$

where ρ is the fluid's density, p is the pressure of the fluid, u is the axial fluid velocity, t is time, and x is the longitudinal distance, which is based on the long-wavelength approximation to the Navier-Stokes equations. The second governing equation is the continuity equation

$$\frac{\partial A}{\partial t} + \frac{\partial Au}{\partial x} = 0 \tag{3}$$

with A equaling the cross-sectional area of the collapsible tube. The quantity Au is equal to the flow rate of the fluid through the collapsible tube, with u representing the longitudinal velocity. The fluid velocity, fluid pressure, and the cross-sectional area are functions of the longitudinal distance and time. The pressure differential with respect to the longitudinal distance is considered a known quantity for the purpose of this explanation.

Eq. (2) and (3) need to be closed by a model for the tube wall. This gap can be covered by tube law. A different form of Eq. (1) is

$$p_{tm}(x,t) = \tilde{P}(A(x,t),x) \tag{4}$$

where the undeformed cross-sectional area of the tube, A0, is characterized by

$$\tilde{P}(A = A_0) = 0. \tag{5}$$

When the flow is steady, the first term of the left side of both Eq. (2) and (3) goes to zero as the flow does not vary with time. Boundary conditions for the flow area include the area being fixed and equal to the initial, undeformed area of A_0 at x = 0 and x = L. When the function has highly positive values for $\tilde{P}$(A) and A, the tube has an axisymmetrically inflated state that looks like a circle, as shown in Figure 1. When the tube is in this state, any deformation comes with stretching of the tube wall. Large transmural pressure changes are needed to force any change in the tube's cross-sectional area when in this inflated state. When the tube is buckled, small changes to the transmural pressure have a large impact on the changes to the cross-sectional area. when the external pressure is sufficiently high in comparison to the internal pressure – resulting

in a highly negative transmural pressure – the opposite walls of the tube touch, as in the lowest sketch of the cross-section within Figure 1 [51]. Limitations exist when using the quasi-one-dimensional equations as many simplifications are made. These equations do not consider the viscosity of the fluid flowing, the impact of the fluid flow in the y- or z-direction, or the three-dimensional deformation of the collapsible vessel. However, simplified quasi-one-dimensional models are useful for gaining a better understanding of the system and its potential outcomes before moving to more comprehensive models.

Collapsible tubes can experience phenomenon such as choking when the tube is sufficiently collapsed, similar to the choked sonic conditions at the throat of a supersonic gas nozzle. Here, choking is referring to the instances when the available area for flow to travel through is reduced, resulting in a jet of faster fluid exiting the constricted area. When steady state is assumed for the flow, the wave speed of small-amplitude disturbances travelling along the tube - also known as pulse-wave propagation – can be defined as

$$c = \sqrt{\frac{1}{\rho D}} \tag{6}$$

where D is the wall distensibility (inverse of stiffness). If the average fluid velocity, u, at the upstream end of the tube is less than the wave speed, c, the collapse of the tube will increase in the direction of the flow. Continuity requires that the flow is then also accelerated in the same direction. If the tube is long enough, a location along the tube is approached where S – which is the speed index (S = u/c) – approaches 1 and the cross-sectional gradient with respect to x approaches infinity. This condition implies that steady flow is no longer possible if the flow rate is large enough that u approaches c at any point along the tube and choking of the flow is happening. If S is greater than 1 at some point within the flow, u is greater than c. Thus, the flow

velocity is higher than the wave speed, making the flow supercritical. Within a quasi-one-dimensional model, a shock-like phenomena would be expected to occur under the supercritical flow conditions. Experimentally, this shock phenomena can be induced by pinching the collapsible tube upstream, forcing a high velocity, and lower wave speed [51].

2.1.2. Material Properties

The material properties assigned to the collapsible vessel were based off a silicone material. The material properties used are shown in Table 1, which are based off literature values for silicone except for the elastic modulus. To determine the elastic modulus of the collapsible tubing, a sample of the tubing was used. The elastic modulus of materials within certain Shore hardness scales can be determined through an approximate correlation of the two properties. Gent, in 1958, proposed the most widely accepted correlation between Shore hardness and the elastic modulus,

$$E = \frac{0.0981(56 + 7.62336S)}{0.137505(254 - 2.54S)} \tag{7}$$

where S is the Type A durometer hardness and E is the elastic modulus in megapascals [52]. The Shore hardness rating was procured using a Rex Durometer specifically calibrated for Shore A hardness. Multiple readings were taken and an average hardness rating of 30.0353 was obtained. After plugging this value into Eq. (7), the resulting elastic modulus was 1.4403 MPa.

Table 1. Material properties used in FEA simulations.

Material Property	**Value**
Elastic Modulus	1.44 MPa
Poisson's Ratio	0.47
Shear Modulus	20 MPa
Mass Density	2,330 kg/m^3
Yield Strength	165 MPa

2.1.3. Experimental Methods

The experimental Starling resistor model used was constructed at North Dakota State University. The base of the pressurized box was built by Custom Plastics, a Fargo, ND company specializing in custom plastic pieces. It was made out of ¼" clear acrylic with the components welded together to prevent leakage. Figure 10 shows the acrylic base with collapsible tubing. The outside of the pressurized box base measures 8.5"x6"x4.25".

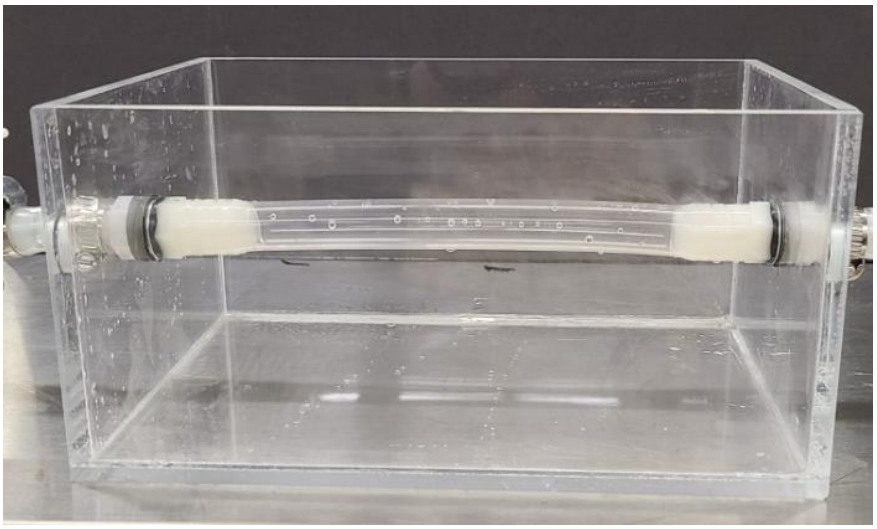

Figure 10. Starling resistor model base with collapsible tube attached.

The acrylic box ends have holes for the barbed fittings that are used to connect the collapsible tubing to the flow loop. Gasket material was sandwiched between the base and top to seal the connection. The top cover was made of ½" clear polycarbonate and has taps for pressurizing equipment and pressure monitor. Metal plates sit above and below the box to provide support and the necessary weight to seal the gasket material. They are connected using threaded rods. Thumb nuts were used to apply pressure to the top plate down onto the polycarbonate and gasket material. The threaded rods ran to self-leveling feet to ensure the Starling resistor remained level. Figure 11 shows the completed Starling resistor model.

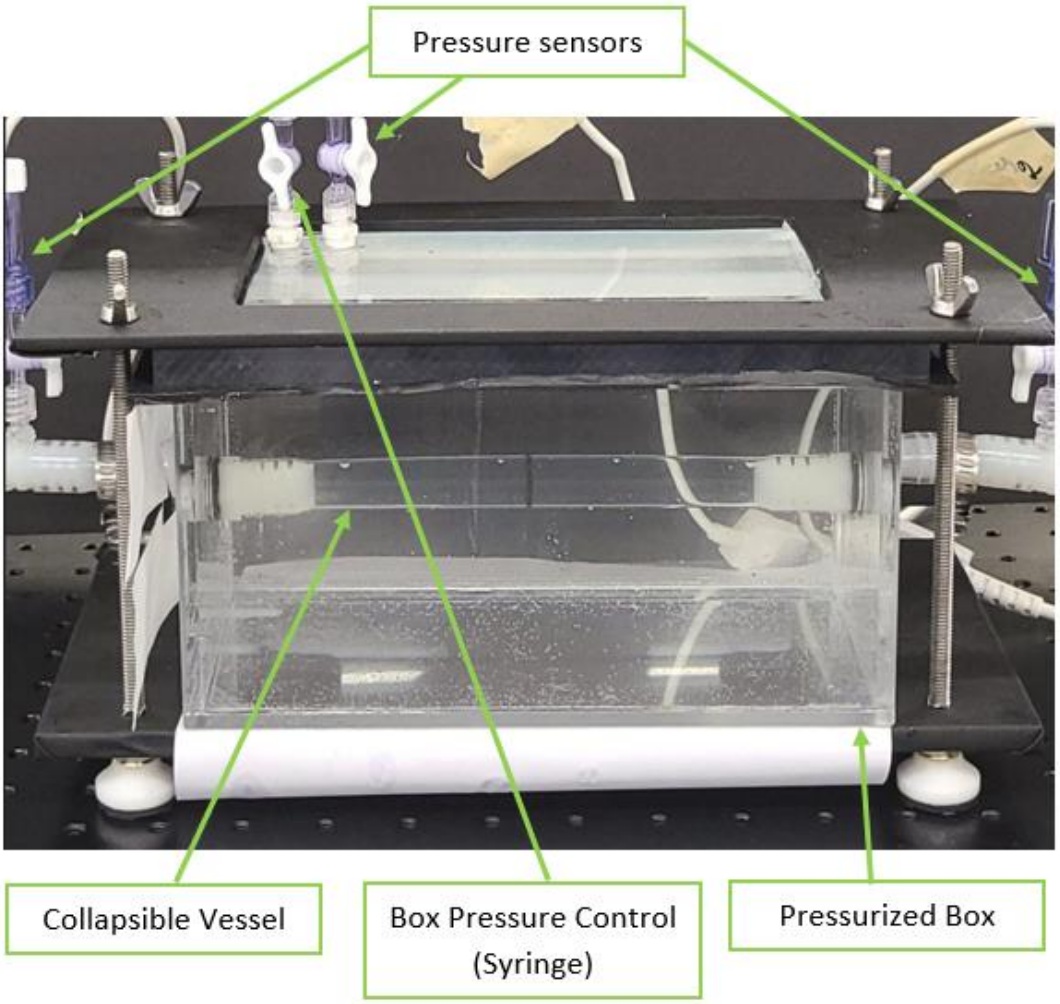

Figure 11. Completed and assembled Starling resistor model.

The collapsible tubing was made of silicone. Its total length was 187.4 mm with an unsupported length of 150.5 mm when in the Starling resistor. Its internal diameter was 15 mm, and the wall thickness was 0.7 mm. The collapsible tubing was supported on plastic barbed fittings to connect the tube to the rest of the flow.

For steady flow, the Starling resistor was connected to a flow loop like shown in Figure 12. Fluid flowed from the overflow tank to the pump up to an inlet tank. From there, the working fluid flowed through the collapsible tubing back to the overflow tank. On either side of the Starling resistor, pressure sensors were connected to measure the pressure at the inlet and outlet of the collapsible tube. Imaging and PIV were used to examine the fluid and structure during active flow.

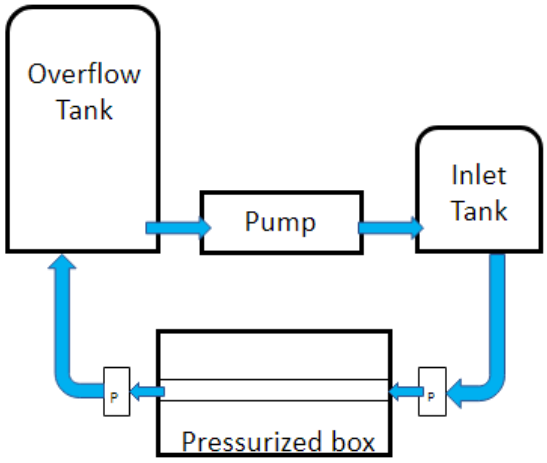

Figure 12. Diagram of flow loop used for steady flow experiments.

The working fluid for both inside the Starling resistor and within the flow loop was a mixture of 40% glycerol and 60% water. This was used as a blood surrogate fluid due to its similar density of 1080 kg/m^3 and viscosity of 3.5 cP. This fluid was also ideal due to it having a matching refractive index with the collapsible tube for optical measurements. Figure 13 shows the comparison between the collapsible tubing filled with air and the tubing filled with the

working fluid. While the tube filled with air clearly shows a distortion of the graph paper beneath the Starling resistor, the tube filled with the working fluid shows almost no disruption of the graph pattern.

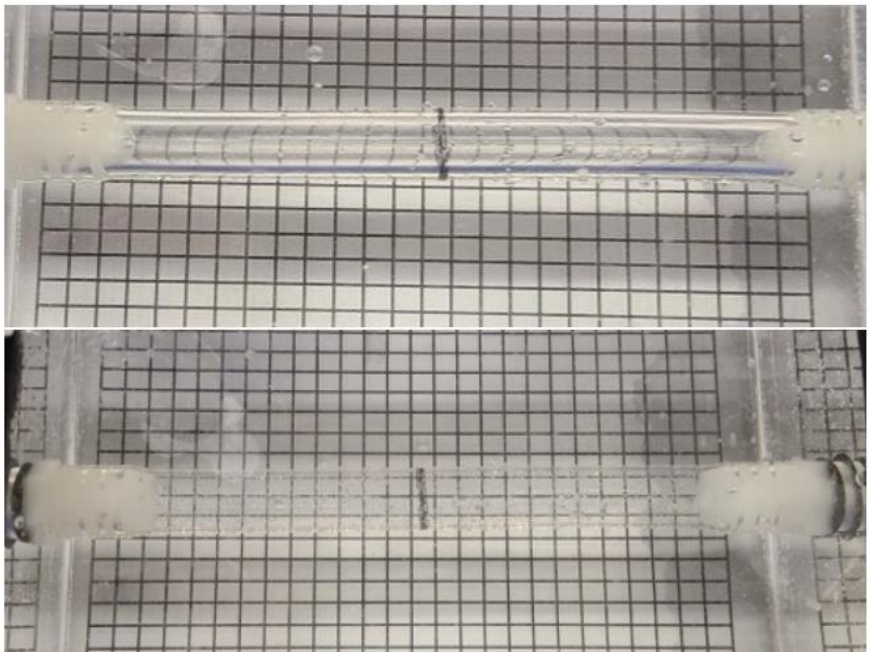

Figure 13. Collapsible tube filled with air (top) and working fluid (bottom).

2.2. Validation of the Local Tube Law

In order to establish the local tube law, the Starling resistor was connected to two longer tubing segments with an internal diameter of 0.25” and a wall thickness of 0.06”. Since tube law is established under no-flow conditions, the resistor was not connected to the entirety of the flow loop. The experimental set up can be seen in Figure 14.

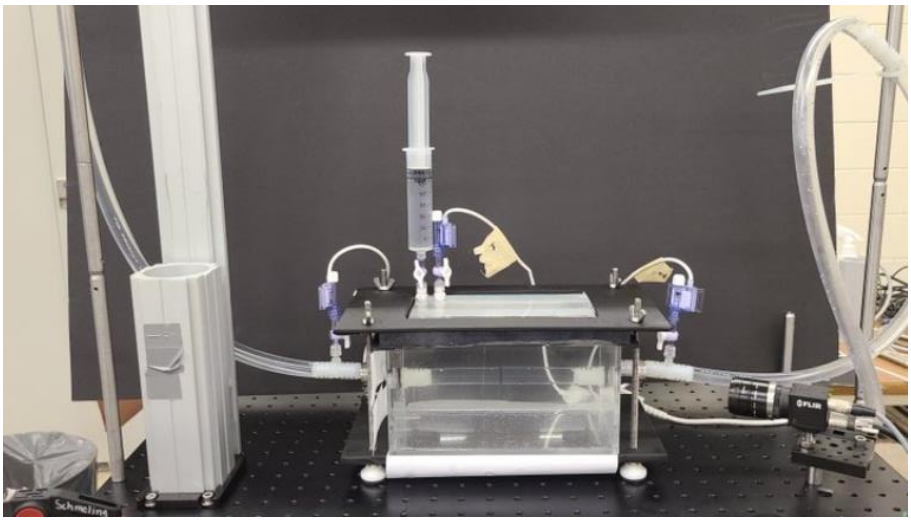

Figure 14. Experimental setup for establish the local tube law.

High-frequency-response pressure sensors (5 kHz) were attached to measure the box, upstream, and downstream pressures. The attached tubing segments were long enough to hold the fluid needed to completely fill the collapsible tube through all phases of collapse. In Figure 14, the camera is seen in the offset side angle, though images were also taken with the camera positioned directly above the Starling resistor to capture the degree of collapse. A circle was drawn at the midpoint of the collapsible tube that enabled the cross-section of the tube to be seen in each image taken in order to track the changes to the cross-sectional area. the camera was angled in order to get a clear image of the drawn circle. The same method was used by Wu et al.; a diagram of their setup can be seen in Figure 15 [25].

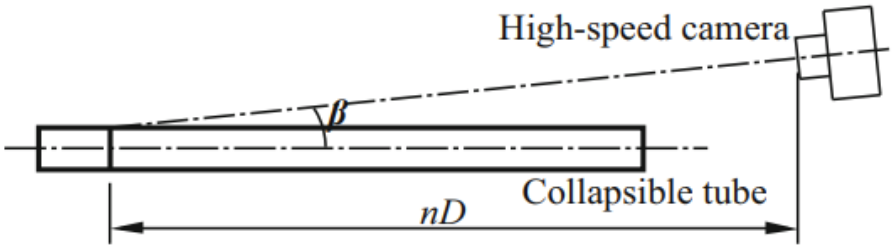

Figure 15. Schematic diagram of the oblique high speed video method. The camera is located at n times the diameter of the collapsible tube, nD away from the drawn circle [25].

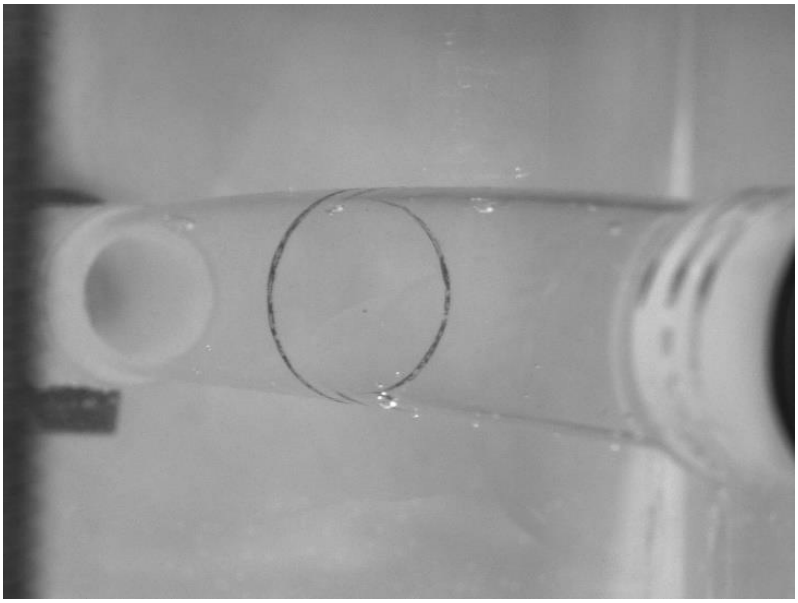

Figure 16. Image taken for tube law establishment with angled camera at zero box pressure.

Pressure readings and images were taken for a series of transmural pressure values from very positive to very negative. Due to the camera being angled, the images taken do not accurately represent the cross-section of the collapsible tube at each transmural pressure. To obtain the actual cross-sectional area, points were placed on the images with a box pressure of zero. The transformation matrix was determined using the equation

$$X = C \times x \tag{8}$$

where X represents the ellipse from the original image, x represents the actual circle, and C is the transformation matrix. The transformation matrix was then applied to the rest of the collected images so that the actual cross-sections are obtained. Figure 17 shows an example of the image captured by the angled camera, the ellipse plotted points, and the transformed circle.

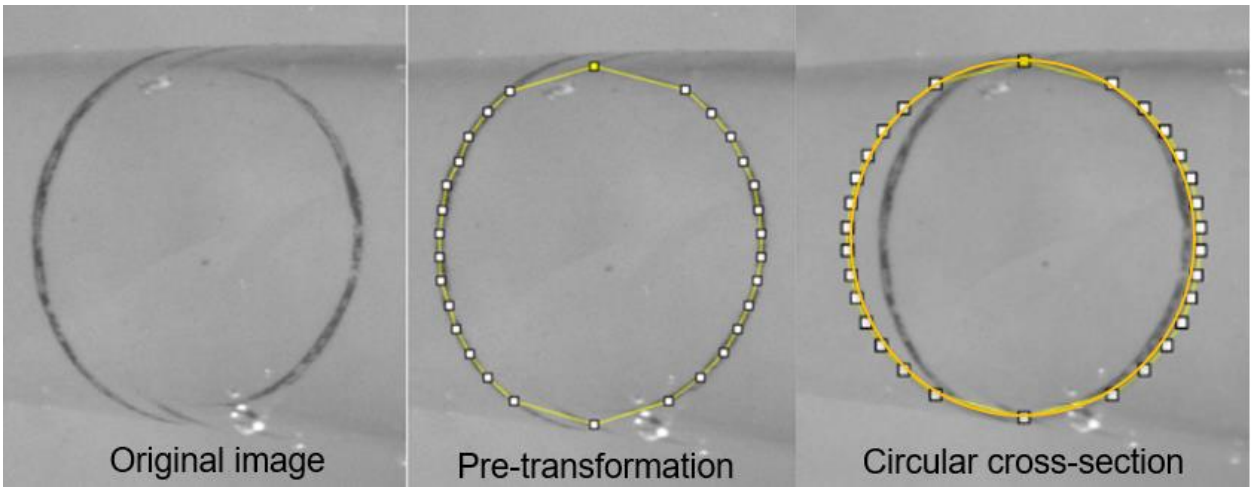

Figure 17. Original image (left), ellipse overlay (center), and obtained circle (right) of a positive transmural pressure case. An orange circle was overlayed onto the plotted points of the right image.

Figure 18 shows the pictures of the drawn circle at the center of the vessel during the transition from positive to negative transmural pressure for the local vessel. To compare our experimental data with existing theoretical models, we convert our measured variable into dimensionless parameters defined in Kozlovsky et al. [39]**.** The normalized cross-sectional area, $\alpha = A/A_0$, was obtained by dividing the measured deformed areas (A) by the undeformed area, which is $A_0 = 176.71\ mm^2$ for our vessel model.

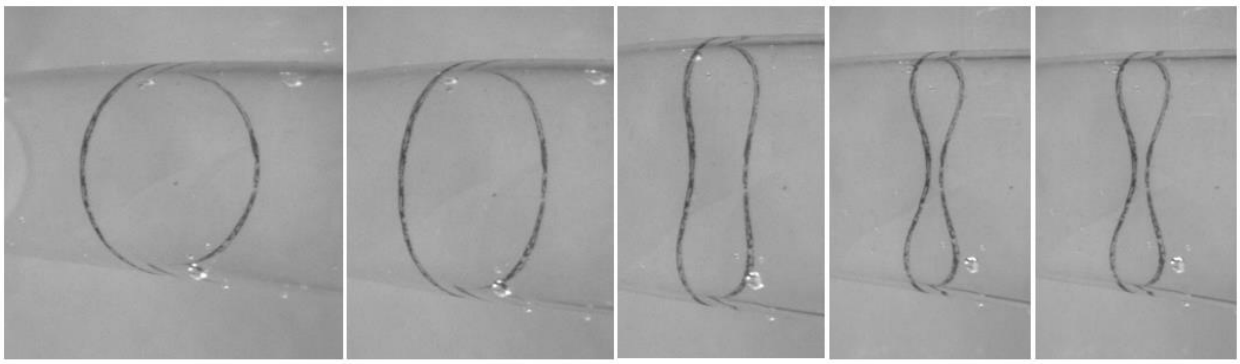

Figure 18. Cross-sections of the collapsible tube with no flow, starting with positive p_{tm} (left) to highly negative p_{tm} (right).

The transmural pressure was normalized using the equation

$$\Pi = \frac{p_{tm}}{K_p} \tag{9}$$

where Π is the normalized transmural pressure, p_{tm} is the experimental transmural pressure in mmHg, and K_p is the flexural rigidity of the tube defined as

$$K_p = \frac{E}{12(1-\nu^2)}\left(ln(1+\gamma)\right)^3. \tag{10}$$

In Eq. (10), E is the Young's modulus in MPa, ν is the Poisson's ratio, and γ is the ratio of the tube's wall thickness to the internal radius. α and Π were then plotted and the results can be seen in Figure 20.

Kozlovsky et al provided an equation that set the normalized transmural pressure (Π) as a function of α and γ, which can be seen below [39].

$$\Pi_{(\alpha,\gamma)} = 3.1\left(\alpha^{{}^{60}/_{\gamma^{0.5}-65}} - \alpha^{0.7\gamma-0.4}\right) \tag{11}$$

The equation was used to compare tubes with different γ values, and the results can be seen in Figure 19.

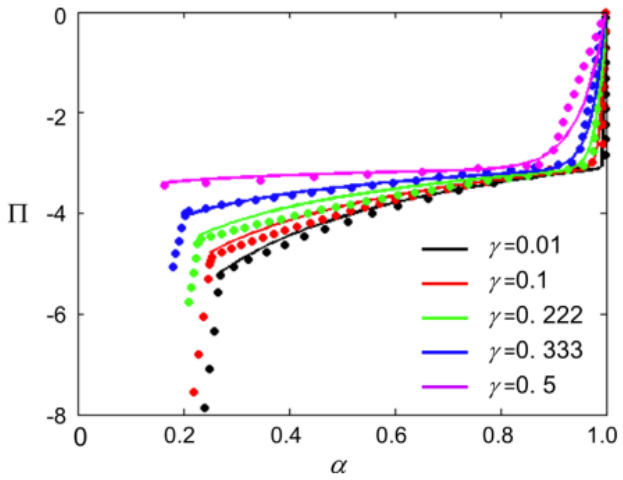

Figure 19. Kozlovsky et al normalized tube law using experimental data and Eq. (11) [39].

The local tube law experimental data points were plotted and used with Eq. (11). The comparisons can be viewed in Figure 20. With the local vessel having a γ of 0.09, there is clear agreement between our local tube law results and the model from Kozlovsky et al [39]. As with Figure 19, the line that resulted from using Eq. (11) in Figure 20 ends around $\Pi = -5$ and data points trail into more negative transmural pressures.

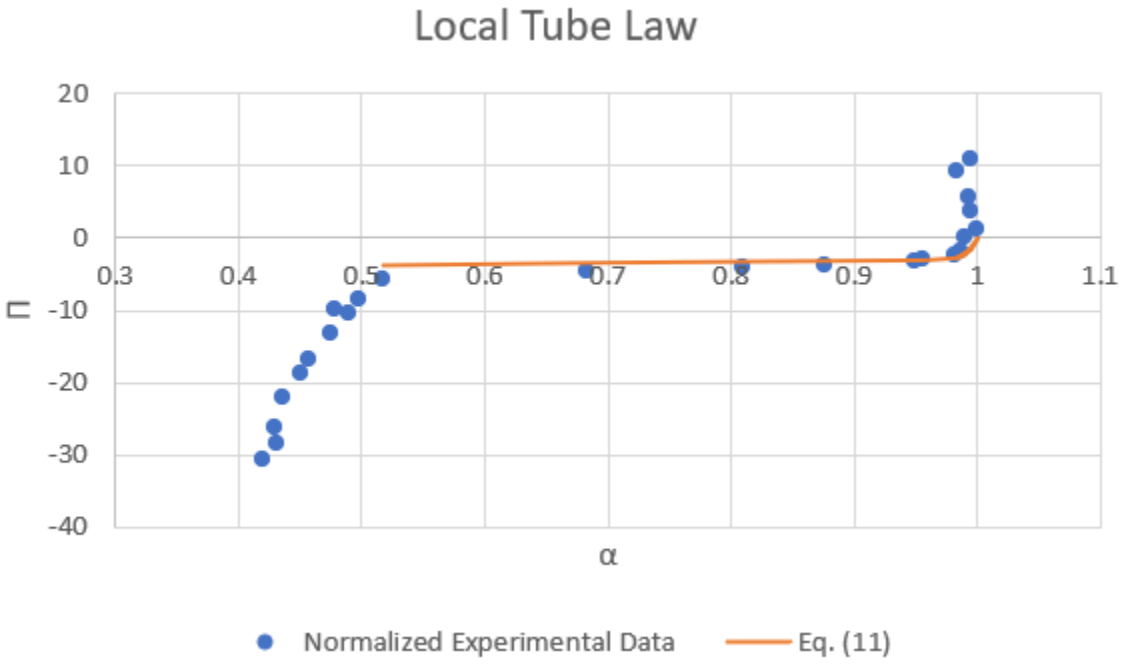

Figure 20. Local tube law shown in normalized experimental data and using Eq. (11) [39].

When compared to the tube law introduced by Shapiro in Figure 1, the local tube law looks very similar, indicating the local vessel follows the traditional tube law. The overall shape is almost identical, with the exception of the highly positive transmural pressures. When the transmural pressure was highly positive, it was expected that the cross-sectional area would be greater than the cross-sectional area when the box pressure was neutral. In practice, this was not found though the areas were also the same comparing to the neutral area. Another area of note is a point with a negative transmural pressure of -9.84 and a nondimensionalized cross-sectional

area of 0.489. It can be seen that this point causes a sharp peak in the negative transmural pressure area of Figure 20. Within this region of the local tube law, the collapsible tubing is highly susceptible to changes in the cross-sectional area with minute changes in transmural pressure.

2.3. Summary

The local tube law, or relationship between the transmural pressure and the cross-sectional area of the tube, was established using a series of pressure readings and their corresponding cross-sections – captured at an angle using a high-speed camera. The experimental transmural pressures and cross-sectional areas were normalized using the flexural rigidity of the tube and the undeformed cross-sectional area, respectively. When these two values were then plotted, the resulting plot was reminiscent in shape to the tube law proposed by Shapiro in 1977 and Kozlovsky *et al* in 2014 [2], [39]. Additionally, with a γ of 0.09, when the local tube law experimental data points are inserted into Eq. (11), the resultant line is as expected and fits with the other γ values used by Kozlovsky *et al*.

3. STEADY FLOW IN PARTIALLY COLLASPED VESSEL

3.1. Experimental Setup

After the local tube law was validated, we examined the steady-flow-induced vessel deformation by connected the Starling resistor to the steady flow loop as shown in Figure 12. The black circle drawn circumferentially around the center of the tube was moved downstream after determining the general shift in the tube's collapse region when flow was introduced to the Starling resistor. The resulting location of the black circle was 30 mm upstream of the downstream barbed hose fitting; this can be seen in Figure 21.

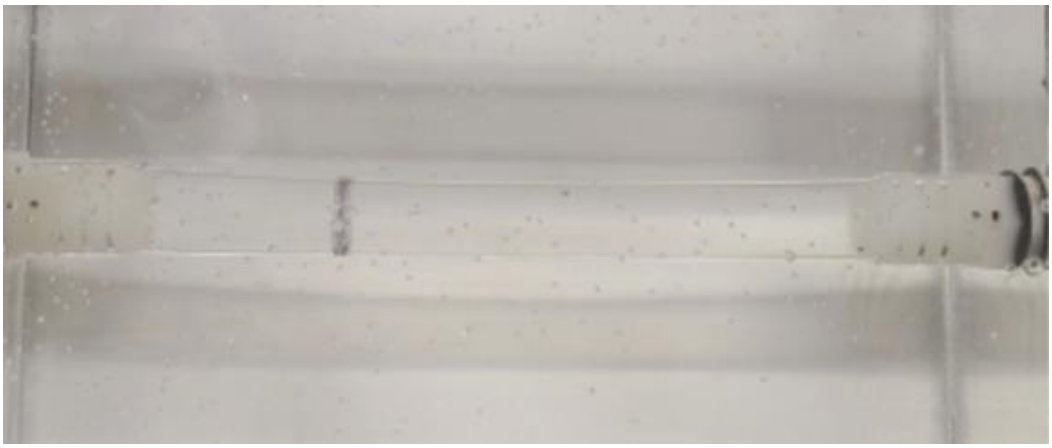

Figure 21. Circle drawn on tube for steady flow experiments. The circle is shifted downstream of the center of the vessel.

Experimental procedure for the steady flow cases involved setting the upstream pressure and flow rate, ranging the transmural pressure from highly positive to negative, and changing the upstream pressure. The downstream pressure level was kept constant for each of the upstream pressure cases. Pressure sensors were used to collect data on the upstream, downstream, and box pressures for each combination of transmural pressure and flow rate; the sampling rate of the sensors was 5 kHz. Transmural pressure is defined as the difference between the box pressure and the downstream pressure reading. The flow rate was collected using a digital flow meter. Images were taken from the same two views as with the tube law – top view and angled side

view. The side view was analyzed in a similar manner to the tube law images with a reference image being chose as the highest positive transmural pressure at the lowest flow rate. This decision was made due to noticing the tube did not expand past the undeformed cross-section in the tube law experiments. The zero-mmHg box pressure case could not be used as with the tube law case due to the flow causing a change in the transmural pressure and a collapse in the vessel at that setting.

The steady flow conditions investigated are: flow rates between 0.33 L/min and 1.72 L/min (Reynolds number between 124 and 636), pressure differences from upstream to downstream of the collapsible vessel of 1.5 mmHg to 11.1 mmHg, and transmural pressures (Π) between 20.17 and -13.12 (16.6 mmHg to -10.8 mmHg). Uncertainties of the experimental results stem from the equipment and measurements taken. The pressure sensors used have an equipment uncertainty of ±2%; the flow meter used has an equipment uncertainty of ±1%. The random uncertainty of the pressure sensor readings was determined using the sample standard deviation; this uncertainty, along with the equipment uncertainty, used the root mean square to determine a range of total uncertainty for the pressure readings taken from the three pressure sensors used. The experimental pressure readings have a total uncertainty range between 0.09 mmHg and 0.90 mmHg; this range is partially due to the differences in sensitivity between the three pressure sensors.

Using 3D modeling software, a model of the collapsible tubing used in the experimental studies was created with a length of 150.5 mm, inner diameter of 15 mm, and wall thickness of 0.7 mm for the finite element analysis (FEA). For the FEA simulation, the external and internal pressure values were set, and the resulting deformations of the tube model were collected. After the tube was modeled, a nonlinear pressure deflection analysis was applied. Fixed connections

were applied at both ends of the tube to simulate the rigid fittings that exist in the experimental model, seen in Figure 22.

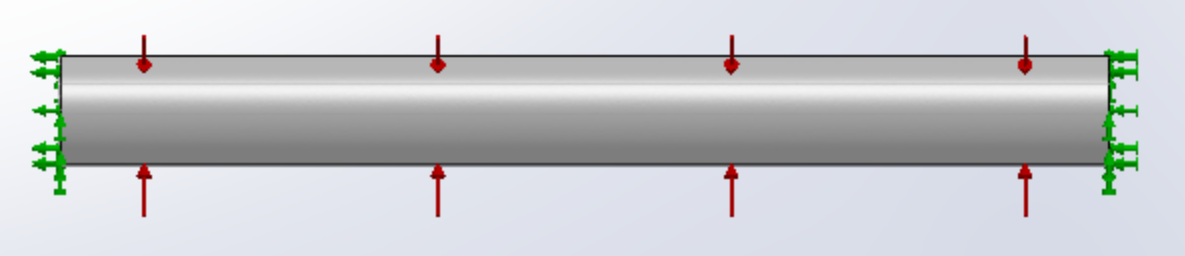

Figure 22. Fixed connections were applied to the ends of the collapsible tube model. Also shown is the constant external pressure applied; not shown is the internal pressure gradient applied.

The mesh applied to the model can be seen in Figure 23. The mesh had a total of 16,016 nodes and 7,982 elements. For each case investigated, a steady external pressure was applied along the tube based on experimental data.

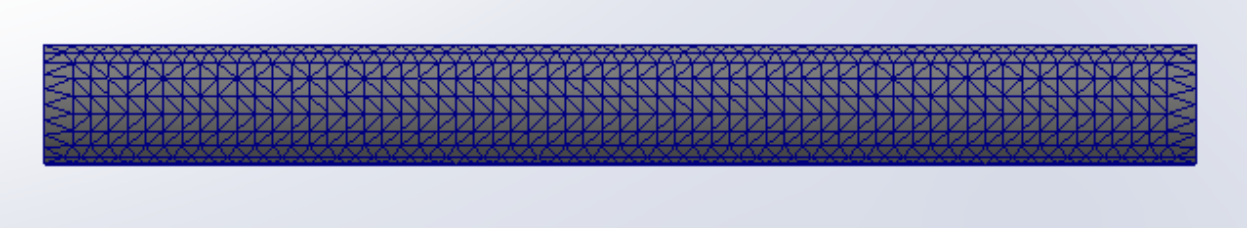

Figure 23. Mesh applied to the collapsible tube model.

A constant inlet pressure along with a pressure gradient was applied was applied to the internal surface of the tube. The internal pressure gradient equation is of the form

$$P(x,y,z) = p * F(x,y,z) = p * (0y + 0z - ax + 1) \quad (12)$$

where P(x,y,z) is the pressure equation, p is the initial pressure at the inlet, F(x,y,z) is the equation of the gradient along the inner tube, and a is the coefficient for the pressure gradient in the x-direction. With flow only in the longitudinal direction, only the x-direction is a concern.

3.2. Results of Steady Flow in the Collapsible Vessel

The collected flow rates were normalized so all collected data could be presented as unitless. This was accomplished by converting the flow rate into the flow's Reynolds number using

$$Re = \frac{\rho u L}{\mu} \tag{13}$$

where ρ is the fluid's density of 1080 kg/m^3, u is the velocity of the flow converted from the recorded flow rate, L is the characteristic dimension of the tubing's diameter at the point of measurement, and μ is the fluid's viscosity of 3.5 cP. The resulting Reynolds numbers reported the expected laminar flow as all were below the transitional threshold to turbulence of 2,100 for pipe flow. The flow was assumed to be fully developed and laminar.

Figure 24 shows a comparison between the side view of the cross-section and top view of the vessel with an initial Reynolds number of 550.7. The first image has a highly positive transmural pressure of Π = 15.80 (13 mmHg), the second a slightly negative transmural pressure of Π = -0.36 (-0.3 mmHg), the third a more negative transmural pressure of Π = -4 (-3.3 mmHg), and the fourth a negative transmural pressure of Π = -10.09 (-8.3 mmHg). This demonstrated the impact of an increasingly negative transmural pressure on the collapse of the tube at a relatively high flow rate.

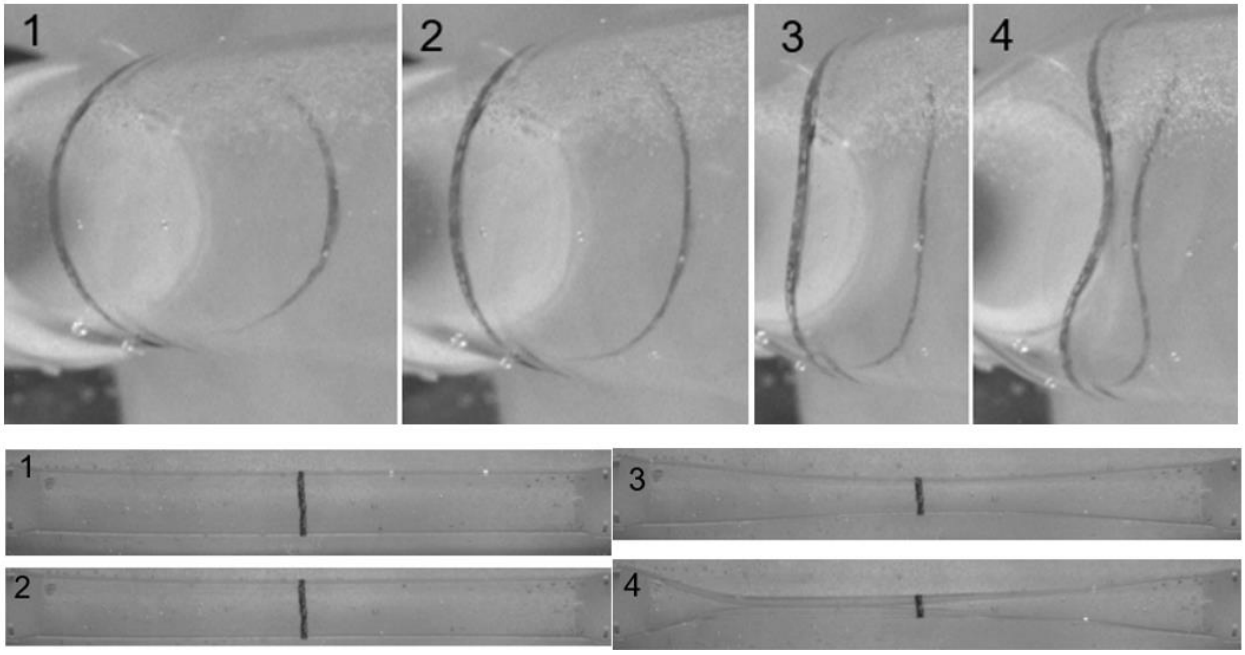

Figure 24. Comparison of side and top view for collapse of vessel with flow with starting Re = 550.7 and transmural pressures of Π = 15.80, -0.36, -4, and -10.09, respectively. Flow moves from right to left.

While the collapse in the second and third images are centered on the tube, the most negative case shows the shift in collapse to downstream of the tube's center. Another example can be seen in Figure 25 where the transmural pressures are Π = -7.53 (-6.2 mmHg) and Π = -8.14 (-6.7 mmHg) for the top and bottom images, respectively. Here, the top collapsed tube has a pressure change of 3 mmHg from upstream to downstream and a Reynolds number of 210 while the bottom has a pressure change of 5.8 mmHg and a Reynolds number of 608.

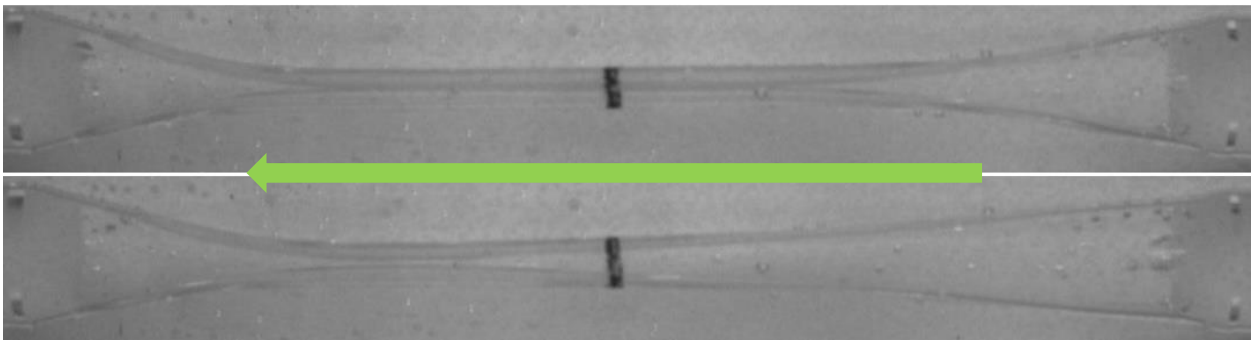

Figure 25. Comparison from center collapse to downstream collapse in vessel. The top image has a Reynolds number of 210, Π = -7.53, and Δp = 3 mmHg. The bottom image has a Reynolds number of 608, Π = -8.14, and Δp = 5.8 mmHg.

When the vessel is subjected to the same transmural pressure and different flow rates, lower flow rates invoke more of a collapse than higher flow rates. This is demonstrated in Figure 26. The transmural pressures of the images range from Π = -4 (-3.3 mmHg) to -4.74 (-3.9 mmHg) and the Reynolds numbers range from 210 to 608. As the flow rate increases, more negative transmural pressure is needed to collapse the vessel to the same degree.

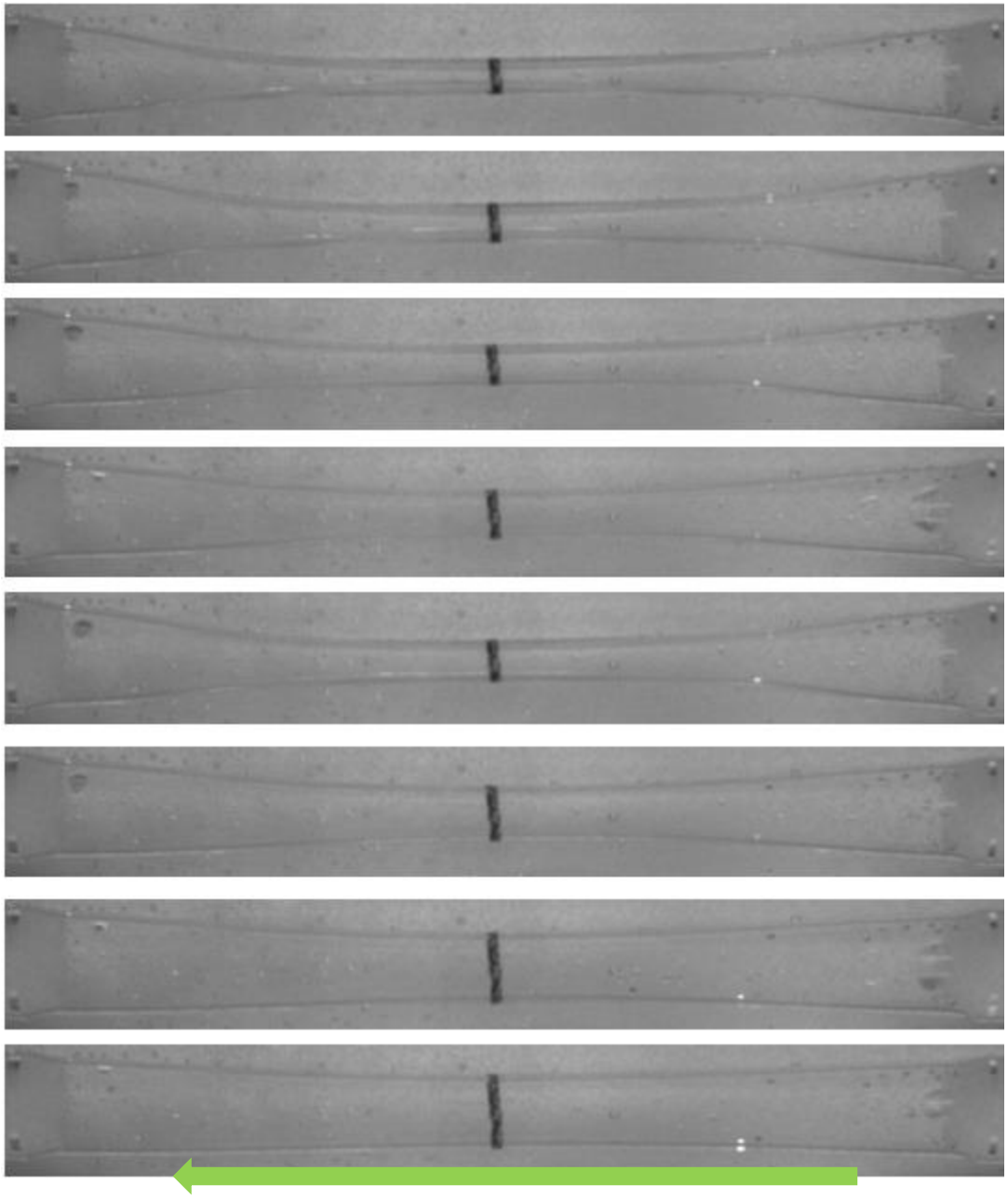

Figure 26. Comparison of collapse at varying flow rates with Reynolds numbers ranging from 210 to 608 and Π = -4 to -4.74.

In the spirit of the local tube law, the normalized transmural pressures and cross-sectional areas at differing initial Reynolds numbers were plotted. Figure 27 shows the Π-α relationship for multiple starting Reynolds numbers. This also shows the correlation between flow rate, transmural pressure, and degree of collapse of the tubing. The lower Reynolds number flows

start collapsing before the transmural pressure becomes negative while the higher Reynolds number flows do not.

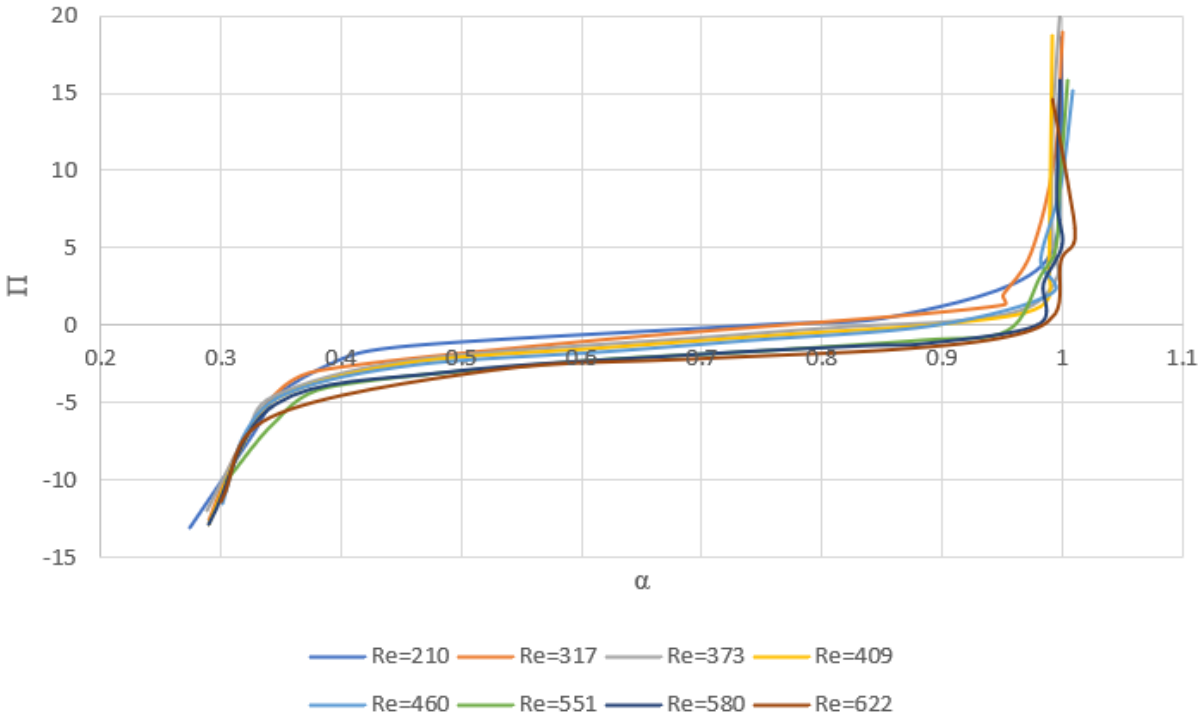

Figure 27. Comparison between normalized transmural pressures Π and normalized cross-sectional areas α at different starting Reynolds numbers.

The lower Reynolds number flows require less negative transmural pressure to collapse – the lowest Reynolds number flows actually start collapsing with slightly positive transmural pressure. As the Reynolds number increased, the less positive and more negative the transmural pressure needed to be in order to collapse vessel. For flow with Π = 0 and Re = 210, the collapse was near the center of the tube and resulted in an elliptic cross-section, as seen in Figure 28.

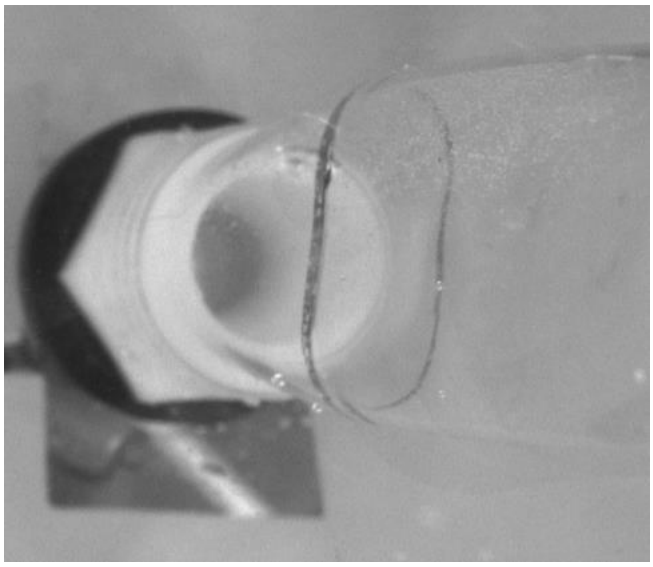

Figure 28. Cross-section of flow case with middle collapse with Reynolds number of 210 and Π=0.

Figure 29 shows the comparison between the experimental collapsing tube and the corresponding finite element result. The collected pressure data from the experimental study was used with the simulations and resulted in a reasonably similar collapse region near the center of the tube. When comparing the normalized cross-sectional area of the experimental collapse to the simulation, the experimental α was 75% and the simulated α was 71%.

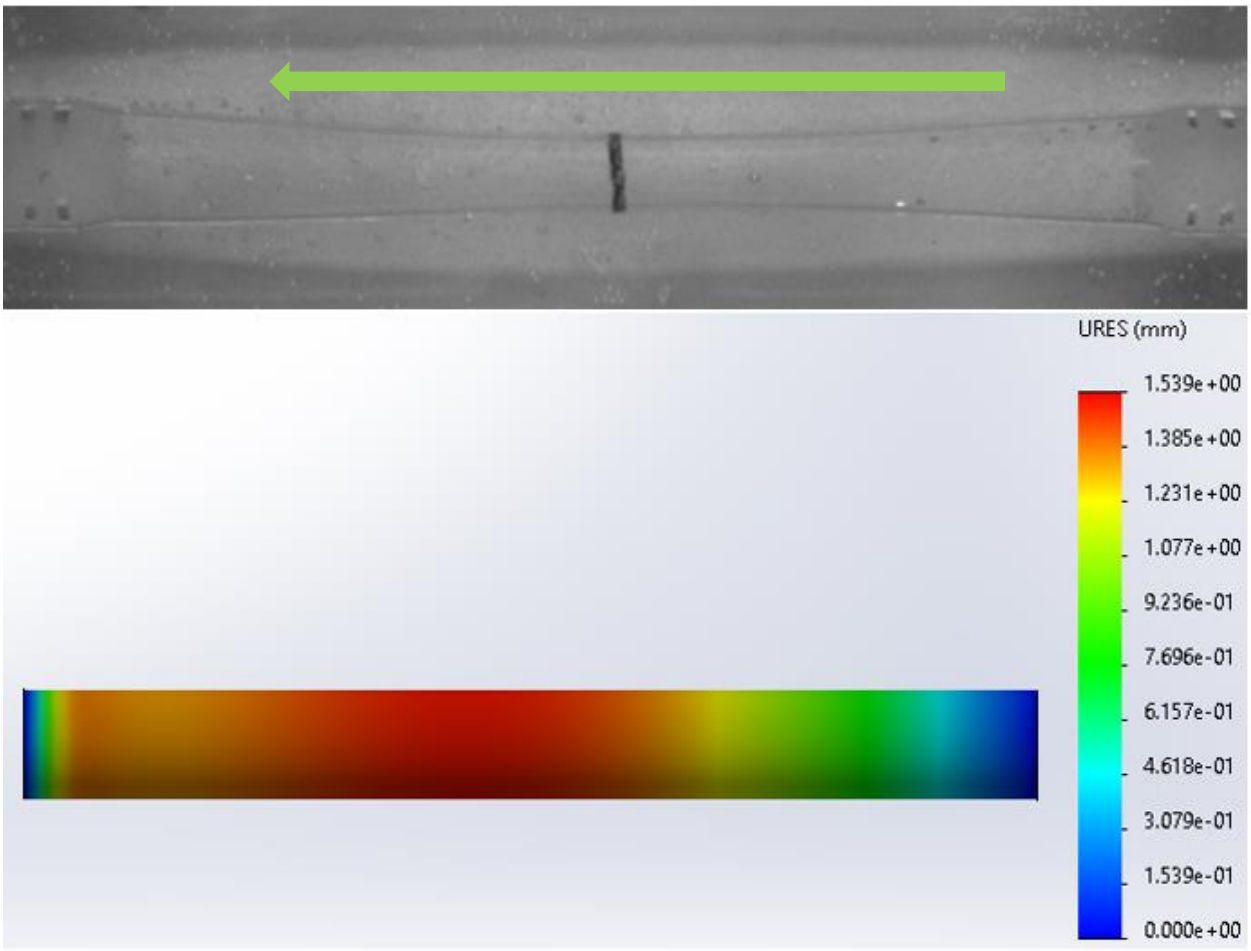

Figure 29. Comparison of experimental to simulation of a middle collapse with Re = 210 and Π=0.

Figure 30 shows the cross-section of a higher flowrate case where the collapse was shifted downstream of the center of the vessel; it is a dumbbell shape due to a more negative transmural pressure of Π = -6.319. The Reynolds number was 547.

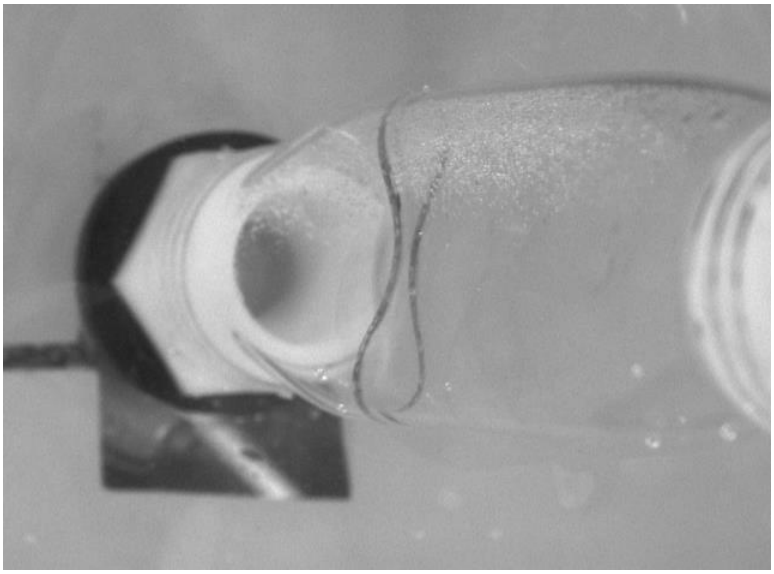

Figure 30. Cross-section of flow case with downstream collapse with Re = 547 and Π = -6.319.

The comparison between the experimental and simulation collapse is shown in Figure 31. Both show a downstream shift from the center of the tube for the collapse, but the simulation's collapse is more concentrated than the experimental. Taking the cross-sectional area at the location of the black circle of both cases, the experimental α was 34% and the simulation's α was 11%. This difference may be due to the concentric collapse of the simulation compared to the experimental dumbbell shape. The axisymmetric nature of the finite element simulation came with limitations on the accuracy of its results when compared to the experimental data. Collapse experimentally was never concentric around the central axis as seen in the simulation, though the effects of the collapse shape are less severe with lower Reynolds number flows. It was assumed for the finite element simulation that the change in pressure is linear, however, due to the flow pattern change in the dumbbell shaped section, the pressure distribution could be significantly varied, which was not simulated in the FEA analysis. This finite element simulation did not consider the impact of fluid through the vessel, only the impact of the pressure along its internal and external walls. A better numerical simulation to employ may be a two-way fluid-structure

interaction that combines the structural analysis of FEA and the fluid flow analysis of computational fluid dynamics. Another limitation of this simulation is the lack of material specific properties for the local collapsible vessel. Due to the destructive nature of many material properties, only the Young's modulus was able to be determined and the other material properties used are based on typical properties for a silicone material. The actual material properties of the collapsible vessel may differ from the assumed properties enough that it would make a significant difference in the results of the FEA simulation.

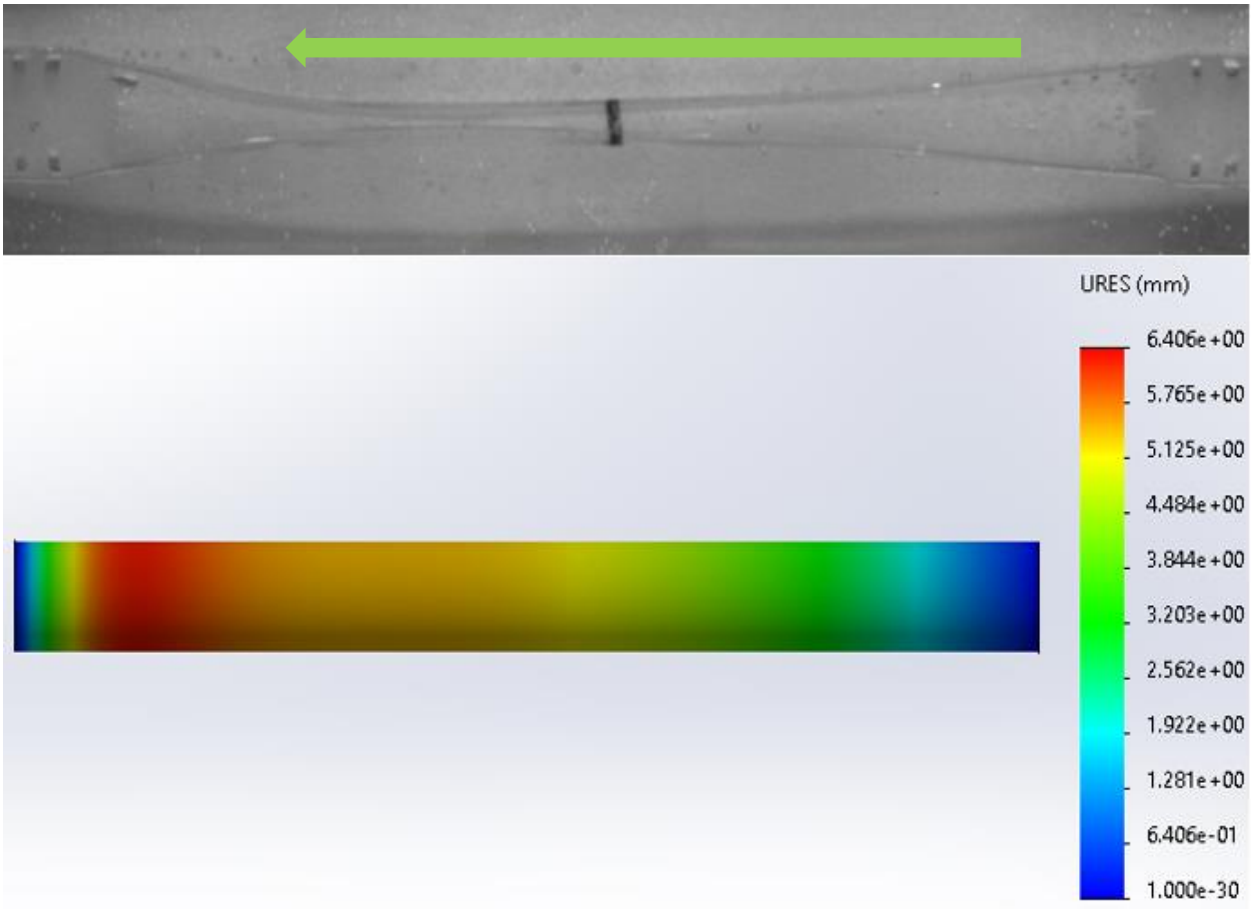

Figure 31. Comparison of experimental to simulation of a downstream collapse with Re = 547 and Π = -6.319.

3.3. Summary

Steady flow was applied to the Starling resistor. Reynolds number and box pressure were varied in order to observe the impact of flow rate on location and degree of collapse. It was found that initially, at lower flow rates, the collapse of the vessel happens at the center of the tube at relatively high transmural pressure. As the Reynolds number increases, the collapse of the tube shifts downstream, to around the area of the black circle drawn circumferentially around the tube and requires lower and more negative transmural pressure to collapse. When the Reynolds number is sufficiently high, the vessel's collapse is the most downstream it will become. This type of collapse appears quite sharply when compared to the other collapse options and does not tolerate a gradual inclination into the shape.

4. SELF-EXCITED OSCILLATIONS

4.1. Experimental Setup

Self-excited oscillations were an area of particular interest when examining the fluid-structure interaction of the collapsible vessel. The search for self-excited oscillations began while investigating steady flow through the Starling resistor. The steady flow loop described in Figure 12 was also used for self-excited oscillations. Higher flow rates than used for the majority of the steady flow investigation was required to induce self-excited oscillations. Self-excited oscillations were achieved when critical transmural pressure values were combined with critical flow rates. This was typically a highly negative transmural pressure combined with a relatively high flow rate. In order to determine the critical values for the transmural pressure and the flow rate needed to both trigger and stop self-excited oscillations, first the box pressure was kept constant while the flow rate was changed to determine a range of Reynolds numbers that could achieve self-excited oscillations. Then, using the determined range as a basis, the flow rate was set, and a range of external pressures were applied in order to determine the range of the transmural pressures that were able to sustain self-excited oscillations at each flow rate.

To better understand the unsteady flow patterns associated with the self-excited oscillations, Particle image velocimetry, or PIV, was used in the present study. PIV utilizes a laser sheet in tandem with a high-speed camera to take images that track the movement of particles within a flow. This allows for the movement of the fluid to be analyzed under different wall conditions. A diagram of a typical PIV experimental setup can be seen in Figure 32; this is comparable to the experimental setup used, though the camera and laser orientations differ.

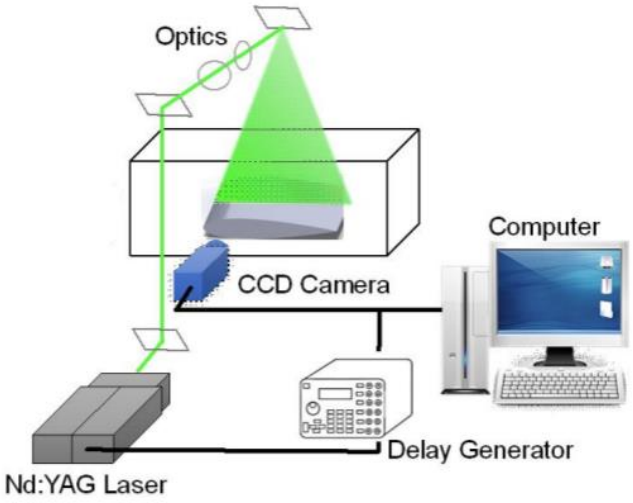

Figure 32. Schematic of a typical PIV setup [53].

The experimental setup can be seen in Figure 33; the laser is on the right and must be refracted through two prisms to be in the same plane as the collapsible tube in the Starling resistor on the right. Here the difference from Figure 32 can be seen; instead of the laser sheet being vertical and the camera horizontal, the laser sheet was positioned in a horizontal orientation and the camera was mounted to provide a top view. This was done due to the orientation of the collapse of the tube; mounting the camera in a top-view orientation allowed for the shape of the tube walls at various stages of collapse to be seen in tandem with the resulting flow movement. The laser beams (532 nm) were shaped into a 1 mm thin laser sheet using a set of spherical and cylindrical optical lenses. A PIV CCD camera (LaVision Imager LX) with a resolution of 1608 × 1208 pixels was installed over the top of the aortic arch model. The CCD camera and lasers were synchronized by a delay generator (BNC Model 577, Berkeley Nucleonic Corp.). In order to track the movement of the fluid, particles were seeded into the flow. The particles used were silver-coated hollow glass spheres with an average diameter of 10 μm. The hollow glass spheres were chosen due to being better suited to the flow and having a better tendency to remain suitably distributed within the flow. The Stokes number for the particle flow

is much less than 1, indicating that the tracers would faithfully follow the flow. For each combination of flow rate and transmural pressure, 150 images were taken using the PIV cameras and pressure data was collected. The delay between images taken varied with differing flow rates but was between 200 and 500 microseconds.

After obtaining the raw images, the vector data were postprocessed using cross-correlation technique (LaVision DaVis software) to compute the instantaneous velocity vectors. A multi-pass interrogation process from a window size of 16 × 16 to 8 × 8 pixels was implemented with an 50 % window overlap.

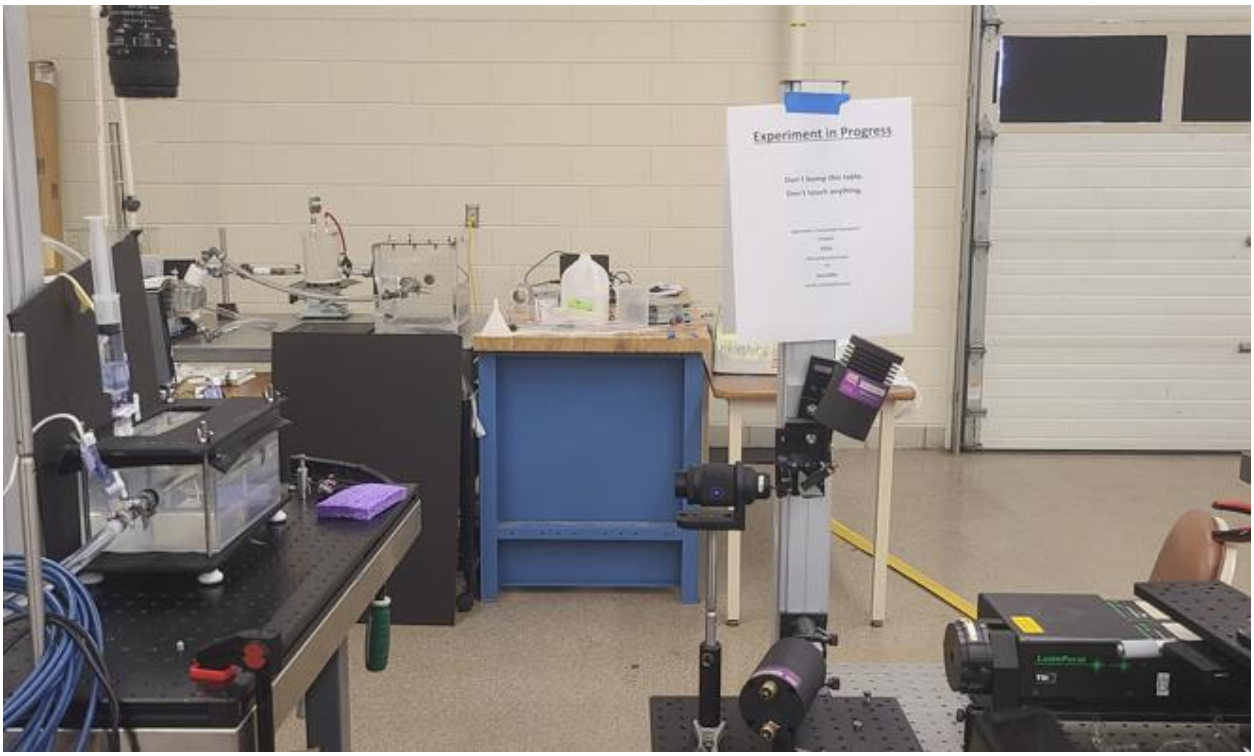

Figure 33. Experimental setup for PIV.

4.2. Results of Self-Excited Oscillation

Self-excited oscillations were found within a range of Reynolds numbers and negative transmural pressures. The required Reynolds number needed to be high enough to shift the

collapse of the vessel from the midpoint and slightly downstream to the most downstream position possible. When box pressure was kept constant at -22.4 mmHg, the critical Reynolds numbers to trigger and terminate self-excited oscillations were determined to be between 1,168 and 1,355. Using this range, the beginning Reynolds number was kept constant, and the transmural pressure was changed to look at the critical values to establish and cease self-excited oscillations. In order to trigger self-excited oscillations, the transmural pressure was needed to be negative enough to collapse the walls of the tube noticeably, but not so much that the opposite walls touched.

Once the cross-sectional variations and region of collapse investigations of steady flow and self-excited oscillations were completed, particle image velocimetry was utilized to examine the fluid-structure interactions of several transmural pressure and Reynolds number combinations. These combinations covered a gamut of collapse states including self-excited oscillations in order to look at a wide variety of interactions between fluid and structure.

Figure 34 shows an oscillation cycle of a flow with a Reynolds number of 1,323 and a transmural pressure of $\Pi = -18.59$ (-15.3 mmHg). The cross-section starts already elliptic before moving towards a dumbbell shape. Once the dumbbell shape is achieved, the cross-section moves back to an elliptic shape. Due to the flow moving through the vessel, the cross-section never reaches a completely circular shape in the region of oscillations, but the opposite walls do not touch either.

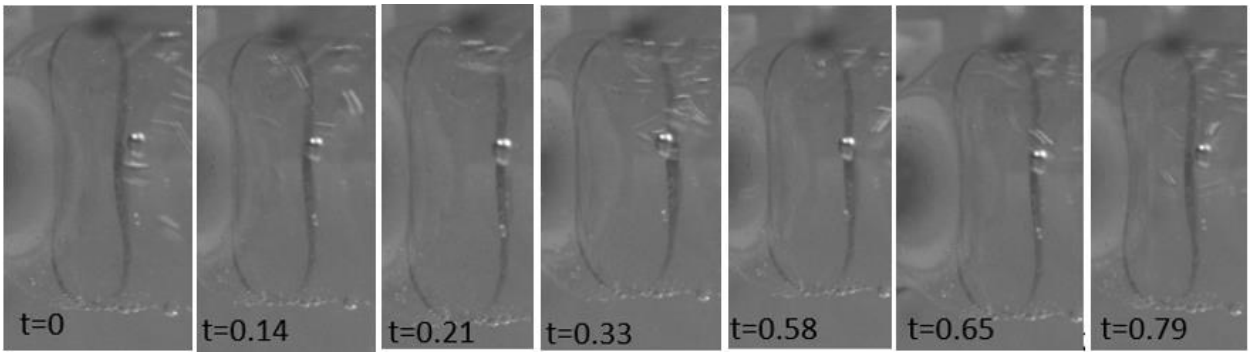

Figure 34. Cross-section of oscillation cycle from flow with Re =1,323 and Π = -18.59 (t=0-0.79 seconds).

Table 2 shows a summary of flow properties for the cases that will be used to discuss the fluid-structure interaction of the working fluid and the collapsible vessel.

Table 2. Summary of flow properties of fluid-structure cases to be discussed.

Case	Q (L/min)	Re	p_{tm} (Π)	Δp (mmHg)	Oscillating?
1	3.75	1,637	-2.92	16.5	No
2	3.74	1,631	-22.12	20.2	No
3	2.88	1,256	-47.03	42	No
4	3.57	1,556	-27.10	23.9	Yes
5	3.40	1,484	-28.92	26.1	Yes
6	3.20	1,399	-40.46	37	Yes

The images collected using PIV were processed using DaVis software from LaVision. A mask was applied to the images outside of the vessel walls to eliminate much of the external noise. The wall of the tube is visible in the images due to the zero-velocity region it consists of.

Flow before the region of collapse was largely consistent in both velocity and flow direction for each combination of Reynolds number and transmural pressure. Regions of discrepancy near the wall may be because of the tendency of the particles to adhere to the inner

wall of the vessel. When flow rates and transmural pressures combined to produce either vessel collapse or self-excited oscillations, flow downstream of the collapse tends to be less uniform, even showing signs of recirculating flow.

Figure 35 shows a raw PIV image and a processed image for an uncollapsed vessel for Case 1, a flow with Re = 1,637 and Π = -2.92 (-2.4 mmHg). The flow is from left to right within the image. The velocity is shown to be relatively straight and uniform through the center of the vessel. The tube wall is at the very edges of the image and has a velocity of zero. The velocity of the flow is seen to be relatively stable through the tube, with an average of 0.5 m/s; pockets of higher flow velocity can be seen. Minor differences in the flow can be seen in the areas near the tube wall, but this may be due to particles sticking to the inner surface of the tube or not making the transition through the plastic fitting at the end of the collapsible tube.

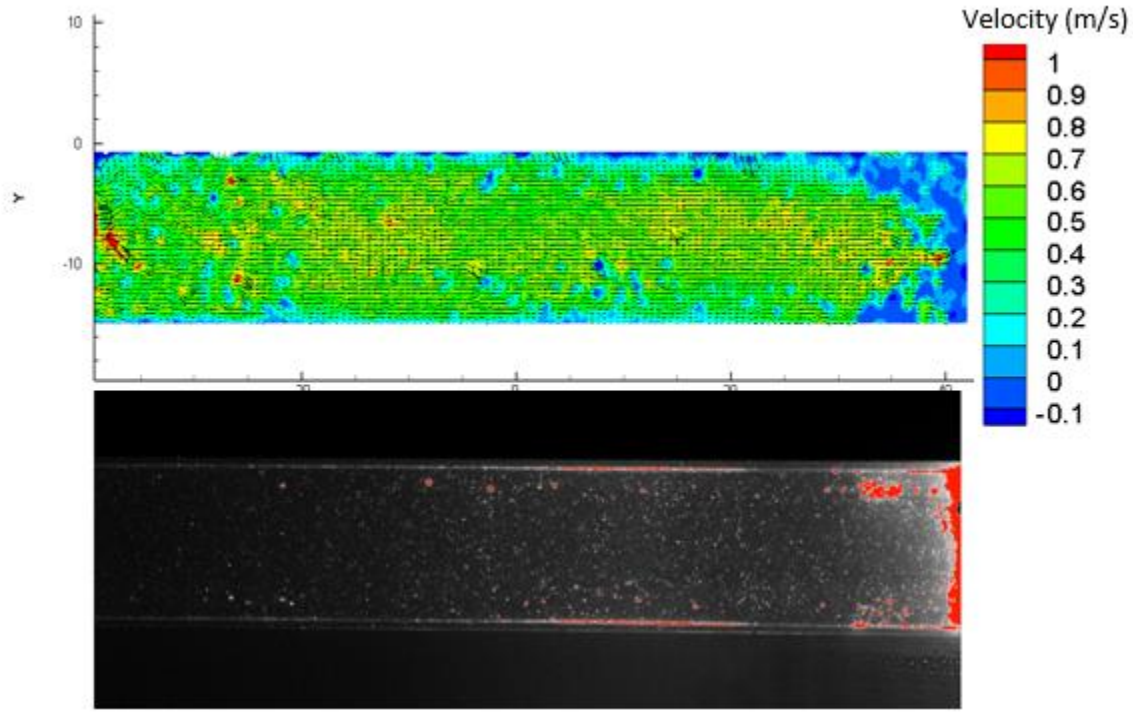

Figure 35. PIV and raw image of Case 1 – uncollapsed tube with Re = 1,637 and Π = -2.92.

When the vessel is partially collapsed, as in Case 2 in Figure 36, an increase in velocity can be seen downstream of the collapse. Here, the flow had a Reynolds number of 1,631 and a transmural pressure of Π = -22.12 (-18.2 mmHg). Upstream of the collapse, the velocity was in the range of 0.4 m/s to 0.7 m/s but increased to 1 m/s through the slightly collapsed region downstream before slowing slightly again as the flow draws away from the collapse.

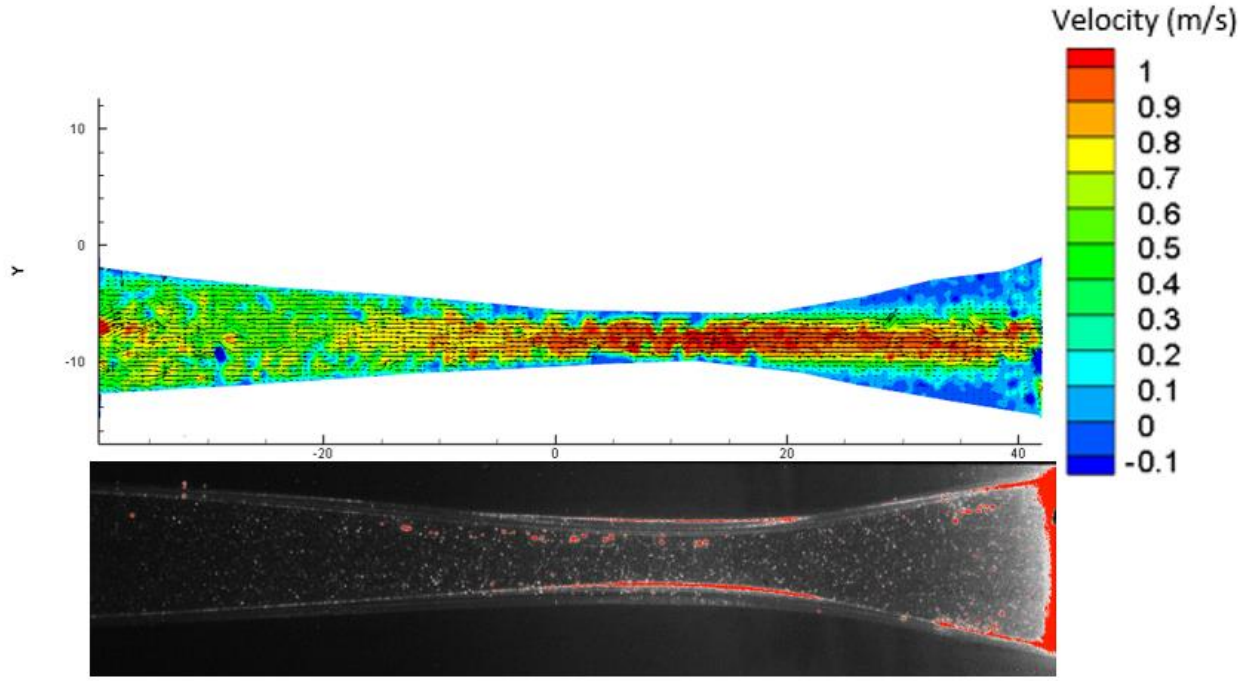

Figure 36. PIV and raw image of Case 2 – partially collapsed vessel with Re = 1,631 and Π=-22.12.

With Re = 1,256 and Π = -47.03 (-38.7 mmHg), Case 3 in Figure 37 shows the vessel collapsed with opposite walls touching but not oscillating. This flow demonstrates a high increase in velocity directly before the collapse; post-collapse, the flow velocity is almost zero with small in the measurement plane due to the dumbbell shaped cross, indicating the fluid is passing through other planes other than the center.

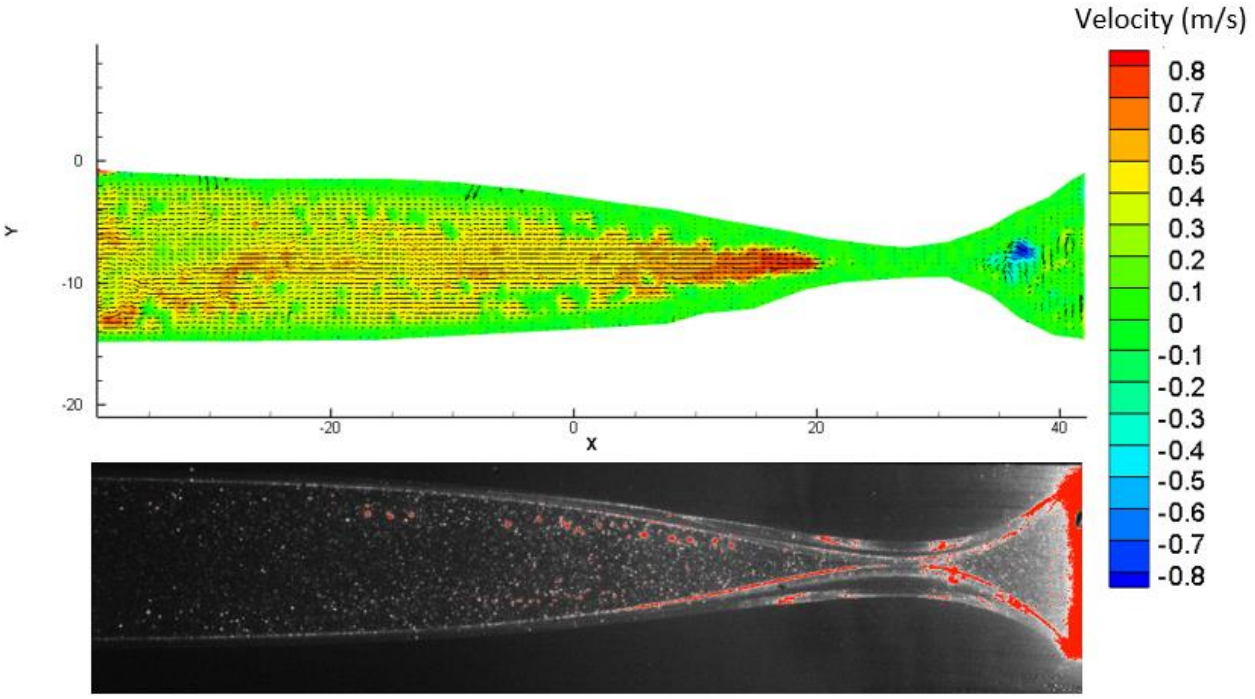

Figure 37. PIV and raw image of Case 3 – totally collapsed vessel with Re = 1,256 and Π=-47.03.

After examining the fluid-structure interaction of various degrees of collapse without oscillations, self-excited oscillations were also explored. Two inlet tank heights were used, resulting in initial Reynolds numbers of 1,648 and 1,637. A range of negative transmural pressures were explored for each Reynolds number to capture the fluid-structure interactions from the trigger of self-excited oscillations to the termination of the oscillations. Figure 38 shows one oscillation cycle for Case 4, a flow with Re = 1,556 and Π = -27.10 (-22.3 mmHg). This flow and oscillation setting was found to be critical to the introduction of self-excited oscillations at the starting Reynolds number. As the walls are barely fluttering, the flow is slightly reacting and changes to the flow velocity can be seen as the higher flow velocity stream moves slightly from the center of the vessel to the sides.

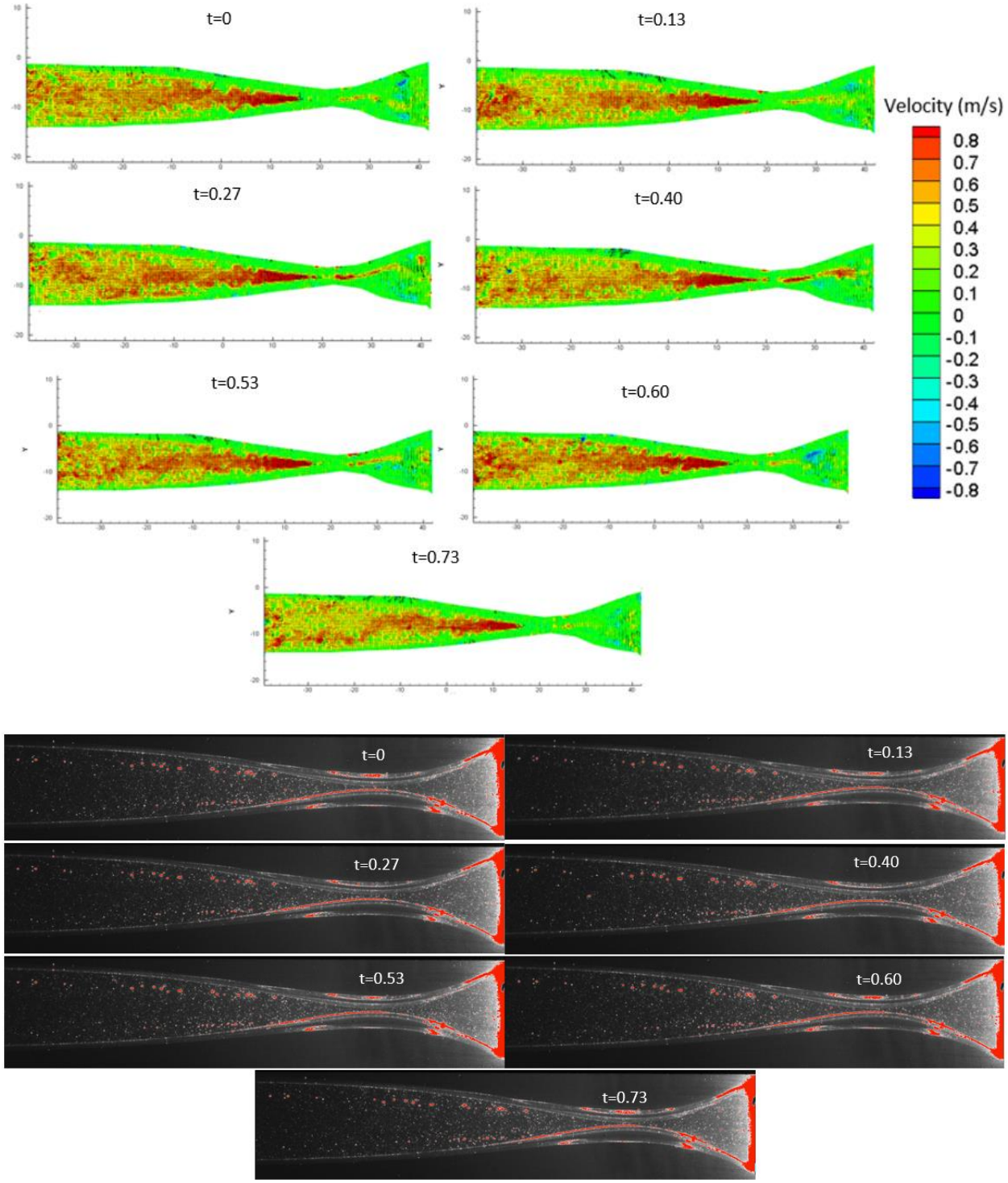

Figure 38. PIV and raw images for an oscillation cycle for Case 4 – flow with Re =1,556 and Π = -27.10.

Figure 39 focuses on the downstream region of the flow past the point of collapse. While the motion of the walls is subtle, the impact on the downstream velocity can be seen in the movement of the direction of the velocity vectors. The main stream of flow post-collapse can be seen moving up and down within the tube and pockets of recirculating flow are hinted at. As the opening becomes narrower and shifts downstream, the stream of higher velocity fluid moves from being centered within the vessel to favoring either the upper or lower region of the post-collapse region; the change from favoring the upper region to favoring the lower changes with alternating oscillation cycles. The overall flow velocity does not vary much but small regions of higher and negative flow can be seen.

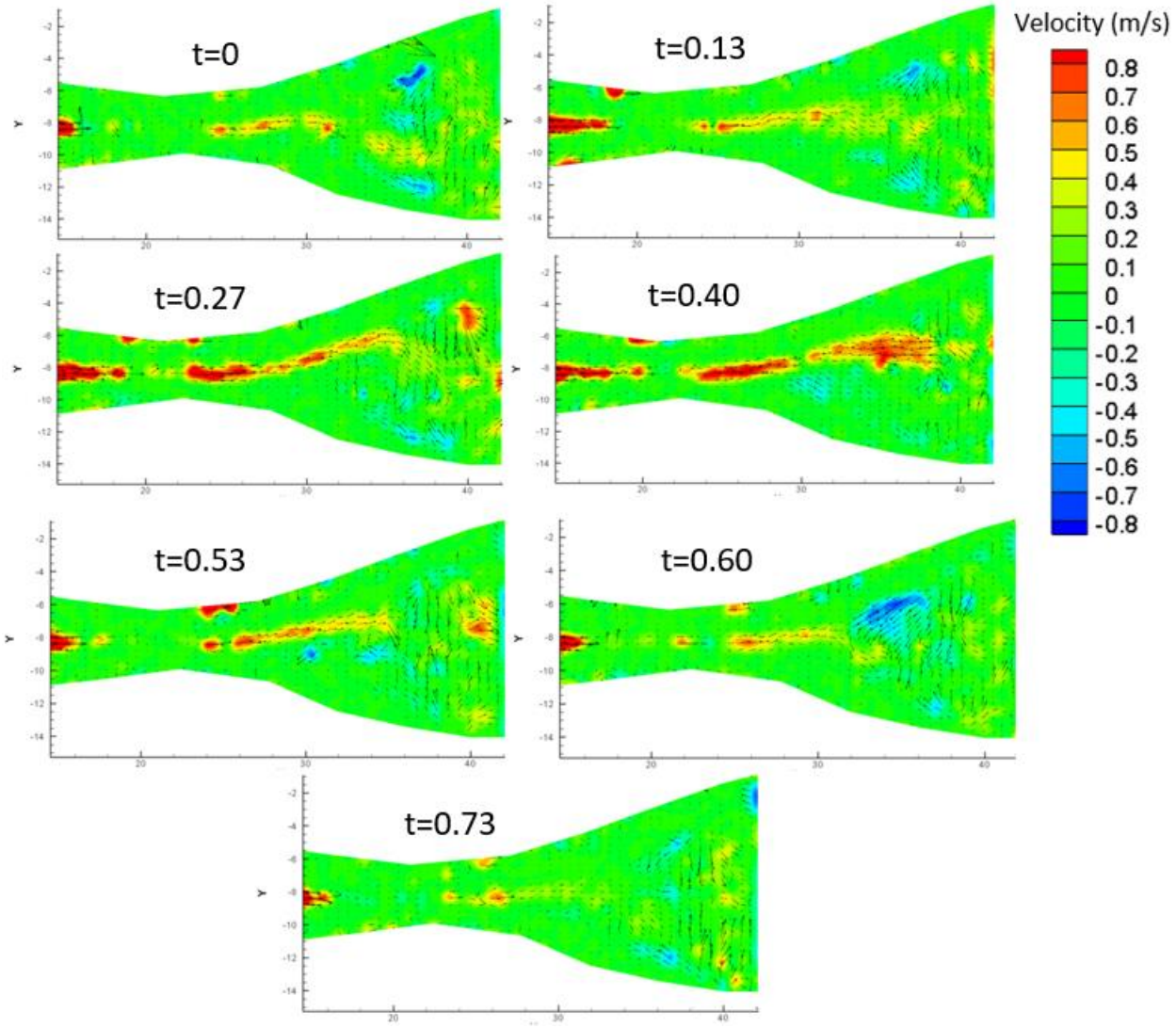

Figure 39. Downstream region of flow with Re =1,556 and Π = -27.10.

Figure 40 shows Case 5, another variety of self-excited oscillations with Re = 1,484 and Π = -28.92 (-23.8 mmHg). As the oscillations occur, the vessel walls shift in two motions – towards each other, almost meeting along the center line, and laterally downstream and upstream. The flow inside reacts to this, resulting in changing velocity and direction of the flow. With differing flow properties, the shift in velocity and direction of the flow is distinct for each oscillation case.

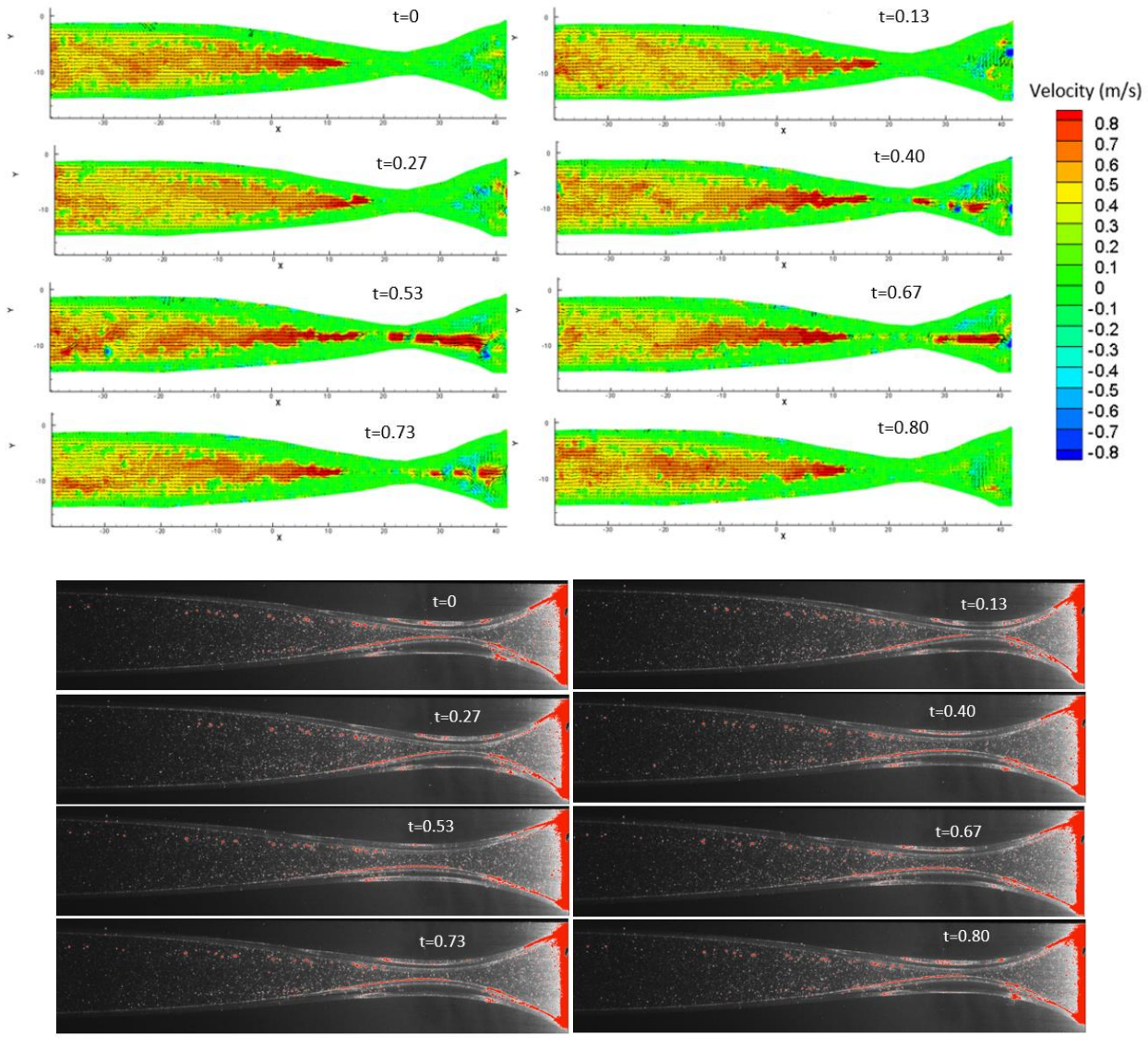

Figure 40. PIV and raw images for an oscillation cycle for Case 5 – flow with Re =1,484 and Π = -28.92.

A focus on the downstream region post-collapse is shown in Figure 41. Similar to other oscillation cases, as the walls open the velocity increases before decreasing as the walls close and the path from upstream to downstream becomes quite narrow to the point of opposite walls touching. Regions of recirculating flow appear with more frequency when the walls of the collapsible vessel are touching and peak in intensity directly after the walls close during the oscillation cycle.

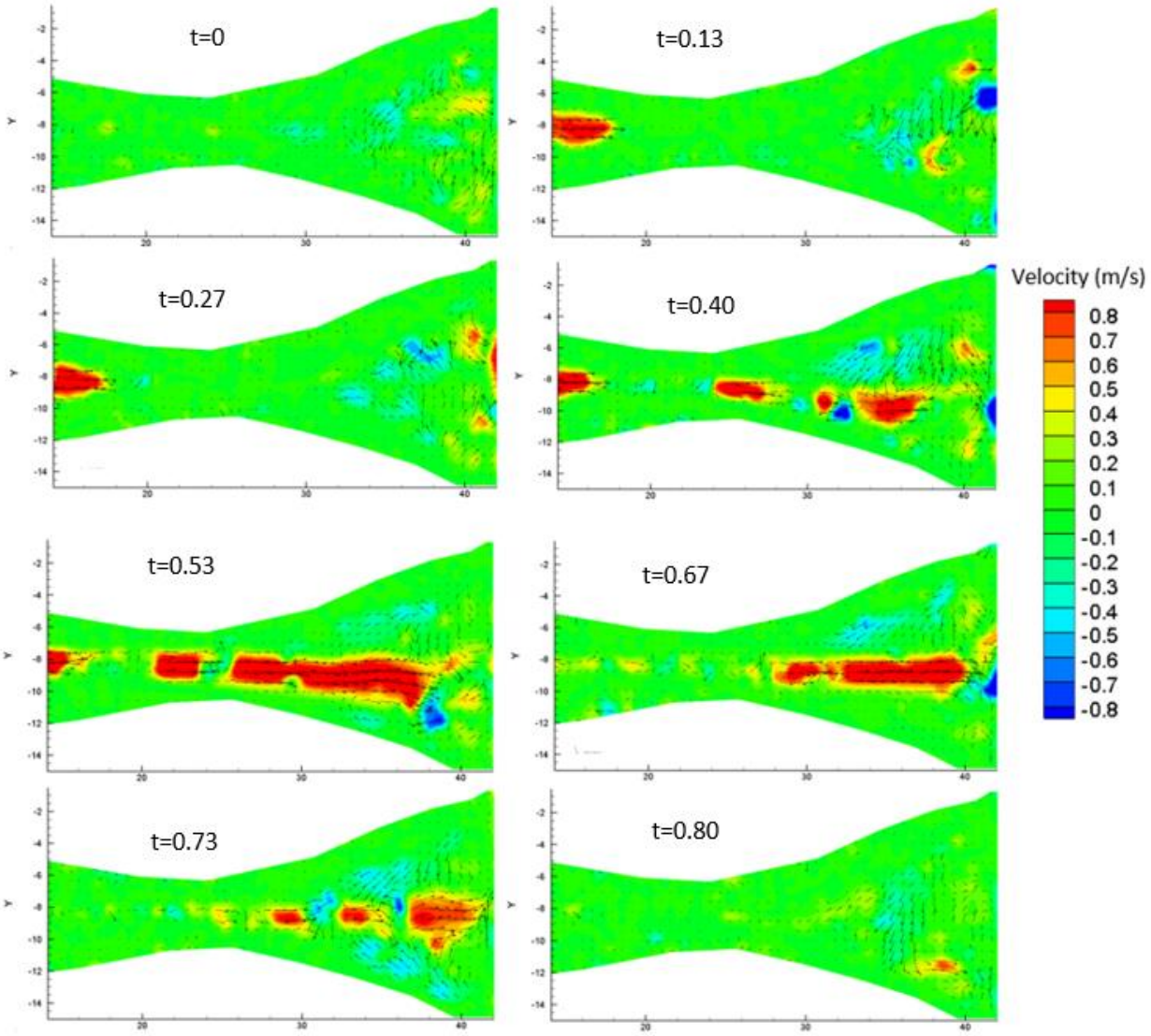

Figure 41. Downstream region of flow with Re =1,484 and Π = -28.92.

Figure 42 shows an oscillation cycle for Case 6, a flow with Re = 1,399 and Π = -40.46 (-33.3 mmHg). This shows the change in fluid flow and velocity as the walls of the vessel collapse during the oscillation cycle. Through the cycle, the walls come together and move slightly downstream before reopening and shifting the collapse region back upstream. The flow velocity increases as the collapse region becomes narrower and reduces in speed as the walls reopen. Regions of negative velocity, or recirculating flow, can also be found during periods of the self-excited oscillations.

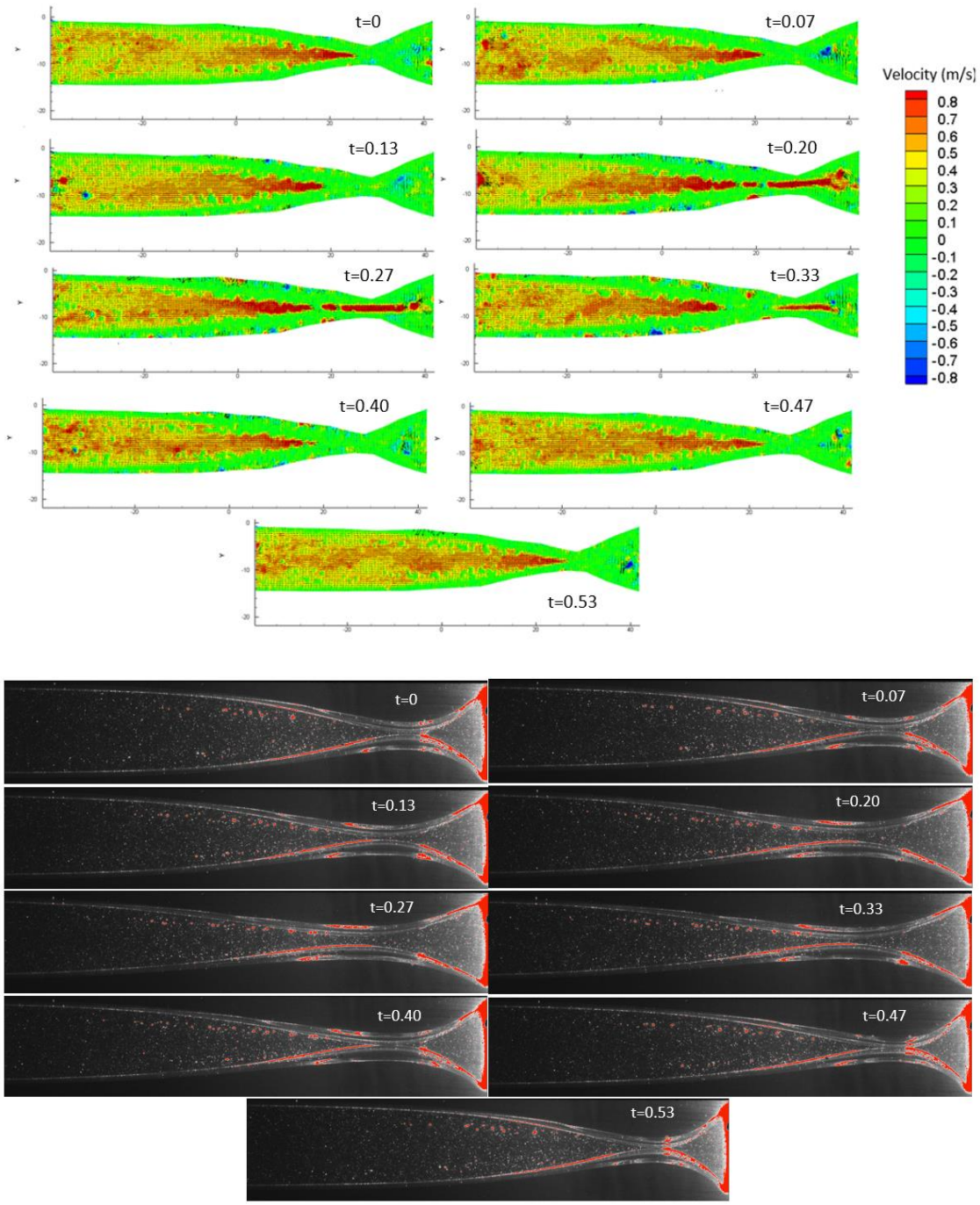

Figure 42. PIV and raw images for an oscillation cycle for Case 6 – flow with Re =1,399 and Π = -40.46.

Figure 43 shows the region downstream of the collapse during the oscillations. This highlights the changes in the velocity and direction of the flow following the collapse of the vessel. As the walls open and the collapse moves upstream, the velocity of the flow increases and

remains relatively straight. As the walls close again and the collapse moves downstream, the velocity decreases and starts to recirculate in several areas within the region.

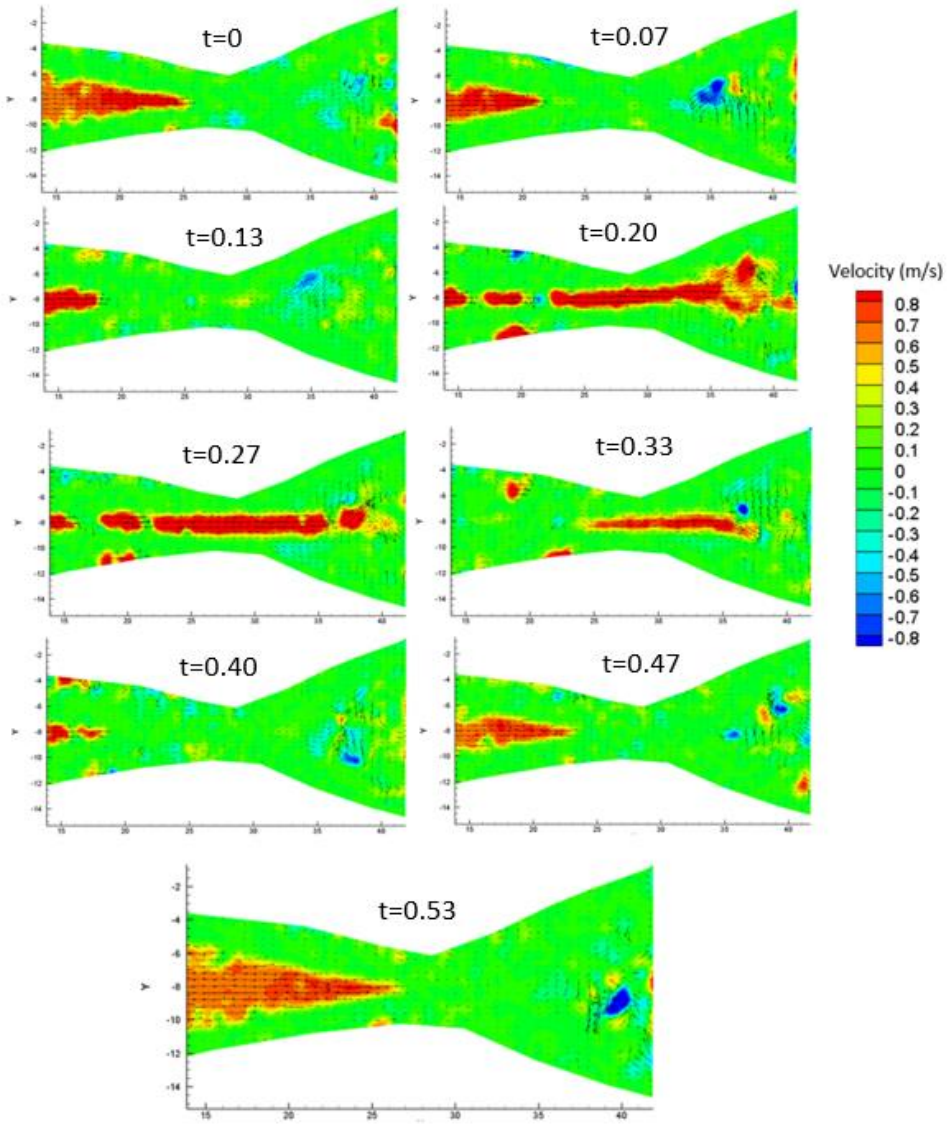

Figure 43. Downstream region of flow with Re =1,399 and Π = -40.46.

The frequency of each of the self-excited oscillations found was determined using Fast Fourier Transform (FFT). Figure 44 shows a sample of the resulting FFT graph; this plot displays 100 of the 75,000 data points available because using all the data points stretches the time on the x-axis and makes the frequency peaks unreadable.

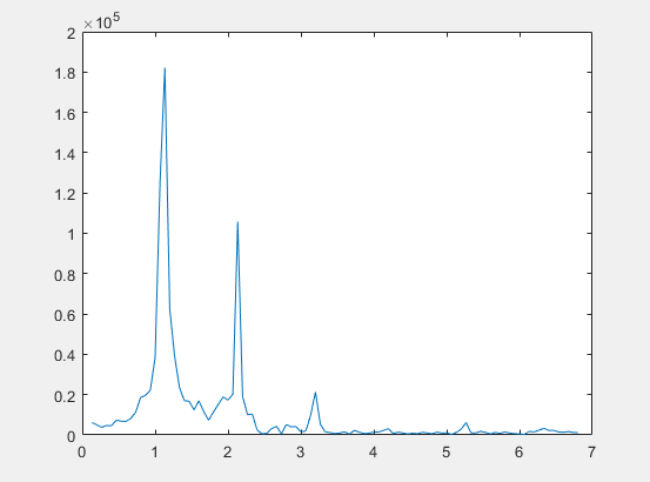

Figure 44. Sample of FFT plot using 100 data points.

It was noted that the frequency of the self-excited oscillations changed. Figure 45 shows the relationship between frequency and Reynolds numbers of the self-excited oscillation cases. The two different colored data markers serve to differentiate between the two sets of experiments conducted at different Reynolds numbers; each of these markers has a unique transmural pressure. As a general trend, the Reynolds number is inversely proportional to the frequency of oscillations.

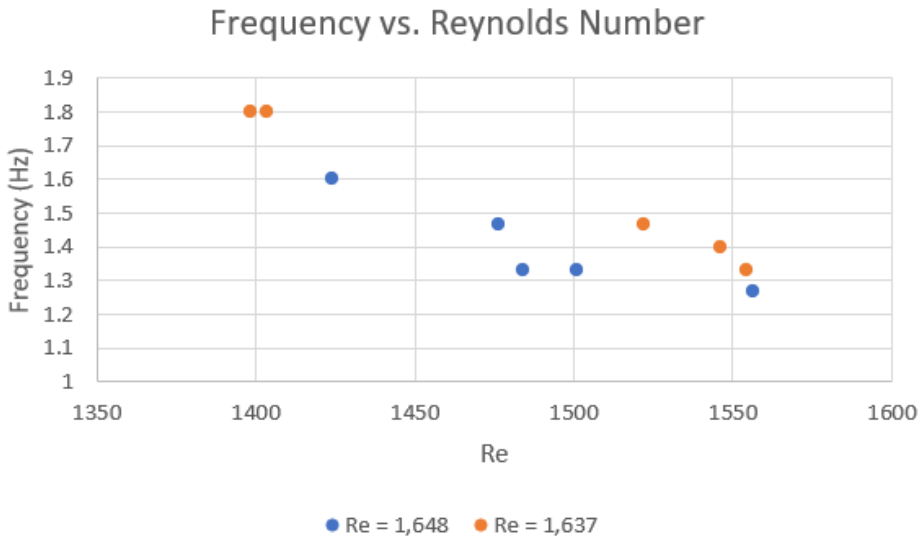

Figure 45. Reynolds number vs frequency for self-excited oscillations.

Figure 46 shows the relationship between the normalized transmural pressure (Π) and the frequency of the same self-excited oscillations. Here, the frequency increases as the transmural pressure becomes more negative. As with Figure 45, the transmural pressure is inversely proportional to the frequency, though there is a stronger correlation between the transmural pressure and frequency than the Reynolds number and frequency.

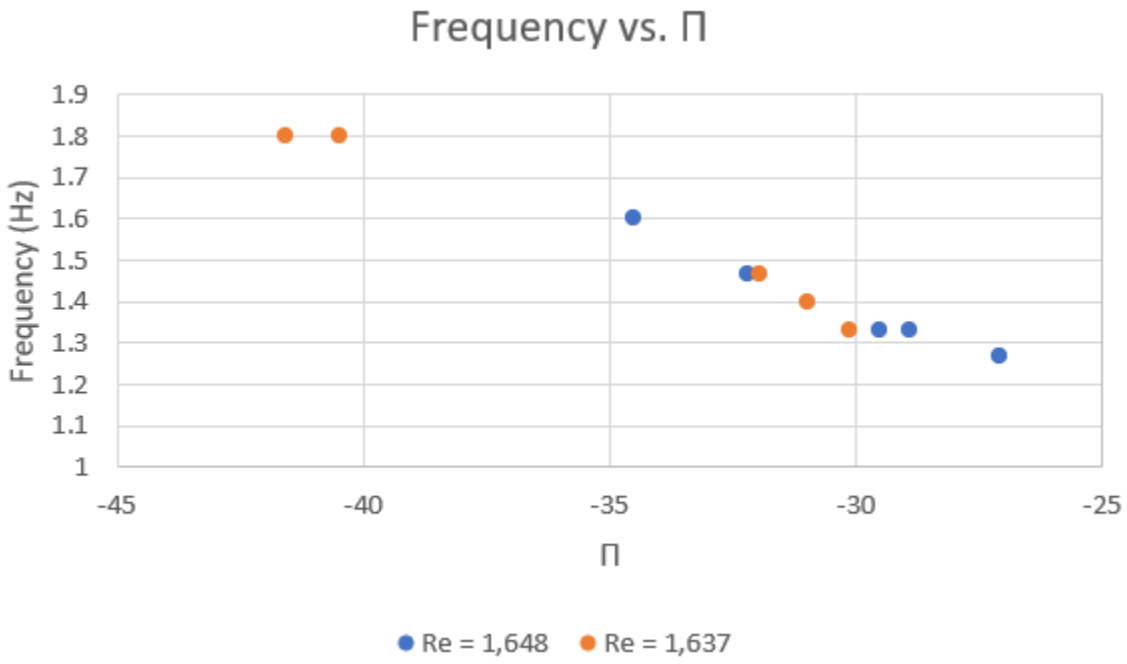

Figure 46. Normalized transmural pressure vs. frequency of self-excited oscillation cases.

The downstream pressure readings were used to construct plots of the oscillations. Figure 47 shows the three downstream pressures plots for the oscillation cases discussed above. The increase in frequency can be easily seen, as well as the different wave shapes for each of the oscillations.

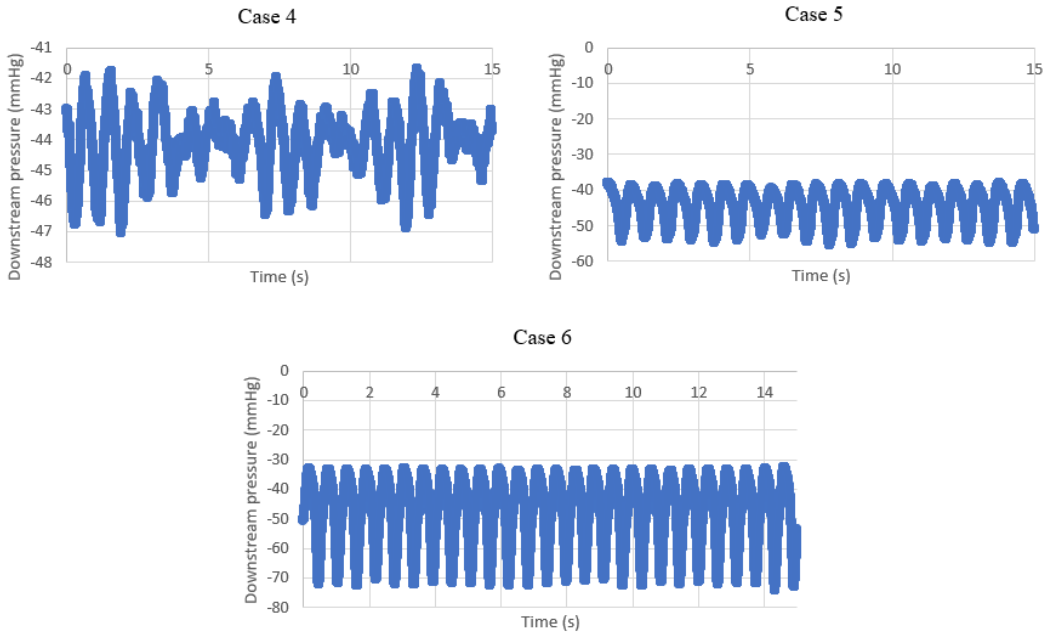

Figure 47. Downstream pressure over time for three oscillation cases.

While Cases 5 and 6 display steady oscillations, Case 6 reflects the unsteady oscillations found at the onset of oscillations at its Reynolds number. This implies that though the most prevalent frequency is the 1.267 Hz previously mentioned, other frequencies may be occurring through the oscillation cycles. Figure 48 compares the results of applying FFT to Case 4 and Case 6.

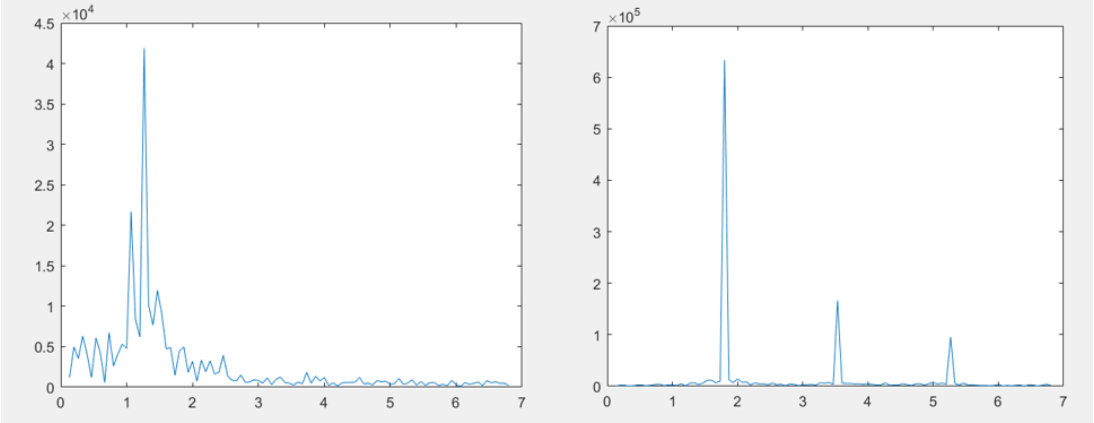

Figure 48. Comparison of FFT results for Case 4 (left) and Case 6 (right).

The Case 4 results show much more noise around the peak frequency than the Case 6 results. This may be due to the less stable condition of the oscillations happening in Case 4.

4.3. Summary

Steady flow was applied to the Starling resistor with higher Reynolds numbers and larger pressure differences from upstream to downstream of the collapsible tube. Self-excited oscillations were found to begin when a sufficient combination of Reynolds number and negative transmural pressure. The Reynolds number needed to be large enough to shift the collapse of the vessel from slightly off-center to completely downstream and the negative transmural pressure needed to be able to cause a collapse that resulted in a dumbbell shaped cross-section without causing the opposite walls of the tube to touch. Using PIV, the fluid-structure interaction of the vessel and the fluid were examined, and it was found that the flow velocity increases as the oscillations cause the walls to collapse but slows as the walls become almost touching, resulting in regions of recirculating flow in the region of the tube downstream of the collapse as well as nonlinear flow directions. Under defined transmural pressures, the frequency of the oscillations was found to increase as the Reynolds number decreased within the region where self-excited oscillations were possible.

5. CONCLUSIONS AND FUTURE WORK

5.1. Concluding Remarks

This thesis presents a comprehensive experimental study of fluid-structure interaction in a thin-walled collapsible vessel. The in-house collapsible tube experiment followed the expected tube law found in literature. The validation of the local tube law was established using normalized transmural pressure and cross-sectional area under no-flow conditions. Positive transmural pressure resulted in a highly circular cross-section. As the transmural pressure became negative, the cross-section descended to an elliptic shape and dumbbell shape before the opposite walls eventually touched. With steady flow, the degree and location of collapse within the vessel is dependent on the transmural pressure and the Reynolds number of the flow. Lower Reynolds numbers resulted in a more centrally located collapse while higher Reynolds numbers shifted the collapse to a region more downstream. The degree of collapse was highly dependent on the transmural pressure. With higher Reynolds number, a more negative transmural pressure is needed to collapsible the tube.

Self-excited oscillations are found to be dependent on critical values of the flow's Reynolds number and transmural pressure. The Reynolds number must be sufficiently large to shift the region of collapse from the center of the tube to a portion of the tube downstream of the middle. The transmural pressure must be negative enough to collapse the vessel, but not so negative that the opposite walls of the vessel touch. Using PIV, the fluid-structure of the flow and the vessel were examined. Flow speeds up past the point of collapse when the tube experiences collapse. During oscillations, flow not only accelerates, but also changes from a linear flow in the direction of the tube to a flow with fluctuating and recirculating flow in the

region downstream of the collapse. Under a certain transmural pressure, the oscillation frequency increases as the Reynolds number decreases within the triggering range.

5.2. Limitations

One of the limitations is the use of the water-glycerol mixture as the working fluid. Since this fluid was chosen partially for its similarity to blood, it is important to note the difference between it and blood. One noteworthy difference is that the water-glycerol fluid is a Newtonian fluid and blood is classified as a non-Newtonian fluid. This means that, while the water-glycerol fluid's viscosity is independent of the shear rate, blood's viscosity changes depending on the stress applied.

Another limitation is with the silicone tube itself. While it is the most basic shape one can attribute to blood vessels, it does not account for any irregularities from a straight, circular tube that may exist in a biological blood vessel. Additionally, the material of the vessel – a silicone rubber – provides the flexibility and motion required for these experiments, but it does not represent the properties of tissues making up blood vessels nor does it consist of biological materials.

The current experimental setup controls the changing of the box and transmural pressure through a syringe to add or remove fluid from the box of the Starling resistor. This relied on the smooth and steady motion of the syringe to change the settings. The syringe motion was not always controlled to be smooth and accurate to achieve the desired transmural pressure.

The finite element simulation is limited by the known material properties of the experimental vessel. Additional material testing to determine more accurate material properties specific to the experimental collapsible tube would add to the specificity and accuracy of the finite element model. The model is limited to circular collapse due to axisymmetric properties

within the software. Additionally, the simulation only accounts for the structure of the vessel, not the impact of flow through the tube.

5.3. Future Work

The current research could be extended in several ways in the future. This could involve rectifying some of the previously mentioned limitations. There are some ideas that could be used to try to expand on the results from Chapter 3 and 4. The following ideas could be used to enhance the already presented results:

1. Improving the method of controlling the box pressure would allow for more regimented exploration of steady flow collapse and critical transmural pressures to trigger and terminate self-excited oscillations. A mechanism that would allow for prescribed changes in the box pressure would allow for more easily repeatable pressure settings. This would apply to all cases with flow applied to the Starling resistor and would add more control to the experiments.
2. Additional material testing would improve the accuracy of the finite element model. However, in order to complete more material testing, the experimental collapsible tube would have to be used, rendering it unusable for further experiments. Further numerical simulations that combine the fluid and structure interaction such as a computational fluid dynamics component would also improve the model.
3. Considering the pulsatile nature of biological blood flow, connecting the Starling resistor to a pulsatile flow loop would provide additional information to add to the knowledge base on the fluid-structure interactions in collapsible vessels. The Starling resistor model connectors has been modified to fit with the existing pulsatile flow loop, which can be seen in Figure 49.

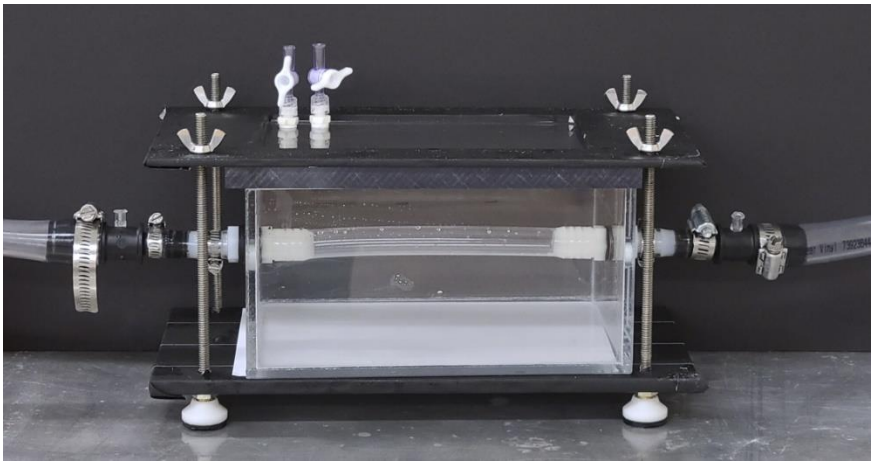

Figure 49. Starling resistor connected to larger diameter tubing used for the pulsatile flow loop.

The connecting tubing from the pulsatile flow loop has an inner diameter of 0.75” and a wall thickness of 0.13” so an appropriate barbed fitting was used to step the diameter down to the size required to connect to the Starling resistor. The pulsatile pump used would be a PD-1100 Pulsatile Pump from BDC Laboratories. The pulsatile flow loop is similar to the steady flow loop, with the exception of an inlet holding tank and the switch from steady to pulsatile pump. A schematic of the pulsatile flow loop can be seen in Figure 50.

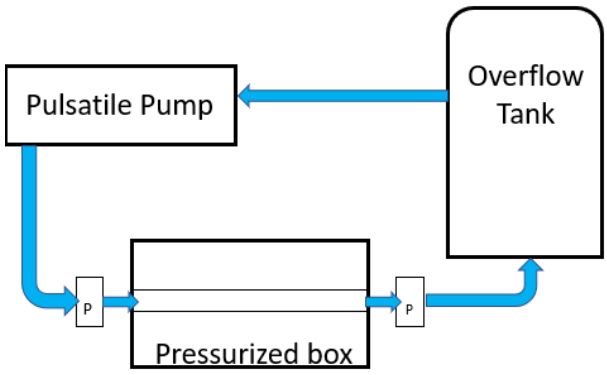

Figure 50. Schematic of the pulsatile flow loop.

Using these ideas, the available knowledge on the fluid-structure interactions of collapsible vessels can be improved upon.

REFERENCES

[1] "Physiology Tutorial - Blood Vessels." http://www.vhlab.umn.edu/atlas/physiology-tutorial/blood-vessels.shtml (accessed Aug. 31, 2021).

[2] A. H. Shapiro, "Steady Flow in Collapsible Tubes," *Journal of Biomechanical Engineering*, vol. 99, no. 3, pp. 126–147, Aug. 1977, doi: 10.1115/1.3426281.

[3] T. J. Pedley and X. Y. Luo, "Modelling Flow and Oscillations in Collapsible Tubes," *Theoretical and Computational Fluid Dynamics*, vol. 10, no. 1–4, pp. 277–294, Jan. 1998, doi: 10.1007/s001620050064.

[4] E. Brøndum *et al.*, "Jugular venous pooling during lowering of the head affects blood pressure of the anesthetized giraffe," *American Journal of Physiology-Regulatory, Integrative and Comparative Physiology*, vol. 297, no. 4, pp. R1058–R1065, Oct. 2009, doi: 10.1152/ajpregu.90804.2008.

[5] J. M. Luce, J. S. Huseby, W. Kirk, and J. Butler, "A Starling resistor regulates cerebral venous outflow in dogs," *Journal of Applied Physiology*, vol. 53, no. 6, pp. 1496–1503, Dec. 1982, doi: 10.1152/jappl.1982.53.6.1496.

[6] "Ernest Henry Starling | British physiologist," *Encyclopedia Britannica*. https://www.britannica.com/biography/Ernest-Henry-Starling (accessed Aug. 31, 2021).

[7] U. F. O. Themes, "Pulmonary Circulation," *Thoracic Key*, Jan. 11, 2017. https://thoracickey.com/pulmonary-circulation-3/ (accessed Aug. 31, 2021).

[8] A. L. Gregory, A. Agarwal, and J. Lasenby, "An experimental investigation to model wheezing in lungs," *Royal Society Open Science*, vol. 8, no. 2, p. 201951, doi: 10.1098/rsos.201951.

[9] "Lumen," *Biology Articles, Tutorials & Dictionary Online*, Oct. 07, 2019. https://www.biologyonline.com/dictionary/lumen (accessed Aug. 31, 2021).

[10] R. L. Binns and D. N. Ku, "Effect of stenosis on wall motion. A possible mechanism of stroke and transient ischemic attack.," *Arteriosclerosis: An Official Journal of the American Heart Association, Inc.*, vol. 9, no. 6, pp. 842–847, Nov. 1989, doi: 10.1161/01.ATV.9.6.842.

[11] C. J. Wiggers, "Circulatory Failure," *Journal of the American Medical Association*, vol. 70, no. 8, pp. 508–511, Feb. 1918, doi: 10.1001/jama.1918.02600080010003.

[12] C. K. Lyon, J. B. Scott, and C. Y. Wang, "Flow through collapsible tubes at low Reynolds numbers. Applicability of the waterfall model.," *Circ Res*, vol. 47, no. 1, pp. 68–73, Jul. 1980, doi: 10.1161/01.RES.47.1.68.

[13] "Blood pressure check: MedlinePlus Medical Encyclopedia Image." https://medlineplus.gov/ency/imagepages/19255.htm (accessed Jan. 25, 2022).

[14] F. P. Knowlton and E. H. Starling, "The influence of variations in temperature and blood-pressure on the performance of the isolated mammalian heart," *J Physiol*, vol. 44, no. 3, pp. 206–219, May 1912.

[15] "Analysis of flow parameters of a Newtonian fluid through a cylindrical collapsible tube | SpringerPlus | Full Text." https://springerplus.springeropen.com/articles/10.1186/2193-1801-3-566 (accessed Jan. 11, 2022).

[16] S. Hayashi, T. Honda, and M. Tanba, "Stability of Steady Flow in Collapsible Tubes," *JSME International Journal Series B*, vol. 37, no. 2, pp. 349–354, 1994, doi: 10.1299/jsmeb.37.349.

[17] W. Lakin, S. Stevens, and N. Thakore, “On the pressure dependence of a Starling-like resistor,” *International Journal of Pure and Applied Mathematics*, vol. 32, Jan. 2006.
[18] S. A. Unhale, G. Marino, and S. Parameswaran, “A One Dimensional Model to Predict Steady Flow Through a Collapsible Tube,” *International Journal for Computational Methods in Engineering Science and Mechanics*, vol. 6, no. 2, pp. 95–103, Sep. 2005, doi: 10.1080/15502280590891573.
[19] O. E. Jensen and T. J. Pedley, “The existence of steady flow in a collapsed tube,” *Journal of Fluid Mechanics*, vol. 206, pp. 339–374, Sep. 1989, doi: 10.1017/S0022112089002326.
[20] X. Y. Luo and T. J. Pedley, “A Numerical Simulation of Steady Flow in a 2-D Collapsible Channel,” *Journal of Fluids and Structures*, vol. 9, no. 2, pp. 149–174, Feb. 1995, doi: 10.1006/jfls.1995.1008.
[21] D. Xu, M. Heil, T. Seeböck, and M. Avila, “Resonances in Pulsatile Channel Flow with an Elastic Wall,” *Physical Review Letters*, p. 5, 2020.
[22] V. S. Yushutin, “Static stability of collapsible tube conveying non-Newtonian fluid,” *arXiv:1412.6397 [physics]*, Dec. 2014, Accessed: Jun. 29, 2021. [Online]. Available: http://arxiv.org/abs/1412.6397
[23] C. Tang, L. Zhu, G. Akingba, and X.-Y. Lu, “Viscous flow past a collapsible channel as a model for self-excited oscillation of blood vessels,” *Journal of Biomechanics*, vol. 48, no. 10, pp. 1922–1929, Jul. 2015, doi: 10.1016/j.jbiomech.2015.04.011.
[24] R.-Q. Wang, T. Lin, P. Shamshery, and A. G. Winter V., “Control of Flow Limitation in Flexible Tubes,” *Journal of Mechanical Design*, vol. 139, no. 1, Oct. 2016, doi: 10.1115/1.4034672.
[25] H.-J. Wu, L.-B. Jia, and X.-Z. Yin, “Experiments on self-excited oscillation in a thin-walled collapsible tube,” *Acta Mech. Sin.*, vol. 31, no. 6, pp. 817–826, Dec. 2015, doi: 10.1007/s10409-015-0465-y.
[26] N. Gavriely, T. R. Shee, D. W. Cugell, James, and B. Grotberg, “Flutter in flow-limited collapsible tubes: a mechanism for generation of wheezes.” 1989.
[27] C. D. Bertram and N. S. J. Elliott, “Flow-rate limitation in a uniform thin-walled collapsible tube, with comparison to a uniform thick-walled tube and a tube of tapering thickness,” *Journal of Fluids and Structures*, vol. 17, no. 4, pp. 541–559, Mar. 2003, doi: 10.1016/S0889-9746(02)00160-3.
[28] M. Heil and S. L. Waters, “How rapidly oscillating collapsible tubes extract energy from a viscous mean flow,” *Journal of Fluid Mechanics*, vol. 601, pp. 199–227, Apr. 2008, doi: 10.1017/S0022112008000463.
[29] L. O. Müller and E. F. Toro, “Enhanced global mathematical model for studying cerebral venous blood flow,” *Journal of Biomechanics*, vol. 47, no. 13, pp. 3361–3372, Oct. 2014, doi: 10.1016/j.jbiomech.2014.08.005.
[30] W. A. Conrad, “Pressure-Flow Relationships in Collapsible Tubes,” *IEEE Transactions on Biomedical Engineering*, vol. BME-16, no. 4, pp. 284–295, Oct. 1969, doi: 10.1109/TBME.1969.4502660.
[31] I. Kececioglu, M. Mcclurken, R. Kamm, and A. Shapiro, “Steady, supercritical flow in collapsible tubes. Part 1. Experimental observations,” *Journal of Fluid Mechanics*, vol. 109, pp. 367–389, Aug. 1981, doi: 10.1017/S0022112081001122.
[32] S. Stelios, “Forced and unforced flow through compliant tubes,” p. 20, 2019, doi: https://doi.org/10.1007/s11012-019-01002-6.

[33] S. Nahar, B. N. Dubey, and E. J. Windhab, “Influence of flowing fluid property through an elastic tube on various deformations along the tube length,” *Physics of Fluids*, vol. 31, no. 10, p. 101905, Oct. 2019, doi: 10.1063/1.5123182.
[34] J. Amatoury, K. Kairaitis, J. R. Wheatley, L. E. Bilston, and T. C. Amis, “Onset of airflow limitation in a collapsible tube model: impact of surrounding pressure, longitudinal strain, and wall folding geometry,” *Journal of Applied Physiology*, vol. 109, no. 5, pp. 1467–1475, Nov. 2010, doi: 10.1152/japplphysiol.00096.2010.
[35] V. Oruç and M. Ö. Çarpinlioğlu, “A test rig for the investigation of airflow through collapsible tubes,” *Proceedings of the Institution of Mechanical Engineers, Part C: Journal of Mechanical Engineering Science*, vol. 221, no. 3, pp. 275–280, Mar. 2007, doi: 10.1243/0954406JMES401.
[36] C. D. Bertram and J. Tscherry, “The onset of flow-rate limitation and flow-induced oscillations in collapsible tubes,” *Journal of Fluids and Structures*, vol. 22, no. 8, pp. 1029–1045, Nov. 2006, doi: 10.1016/j.jfluidstructs.2006.07.005.
[37] R. K. Lambert and T. A. Wilson, “Flow limitation in a collapsible tube.,” *Journal of Applied Physiology*, vol. 33, no. 1, pp. 150–153, Jul. 1972, doi: 10.1152/jappl.1972.33.1.150.
[38] M. Heil and A. L. Hazel, “Fluid-Structure Interaction in Internal Physiological Flows,” *Annual Review of Fluid Mechanics*, vol. 43, no. 1, pp. 141–162, 2011, doi: 10.1146/annurev-fluid-122109-160703.
[39] P. Kozlovsky, U. Zaretsky, A. J. Jaffa, and D. Elad, “General tube law for collapsible thin and thick-wall tubes,” *J Biomech*, vol. 47, no. 10, pp. 2378–2384, Jul. 2014, doi: 10.1016/j.jbiomech.2014.04.033.
[40] C. Melot *et al.*, “Starling resistor vs. distensible vessel models for embolic pulmonary hypertension,” *American Journal of Physiology-Heart and Circulatory Physiology*, vol. 268, no. 2, pp. H817–H827, Feb. 1995, doi: 10.1152/ajpheart.1995.268.2.H817.
[41] M. A. F. Zarandi, K. Garman, J. S. Rhee, B. T. Woodson, and G. J. M. Garcia, “Effect of tube length on the buckling pressure of collapsible tubes,” *Computers in Biology and Medicine*, vol. 136, p. 104693, Sep. 2021, doi: 10.1016/j.compbiomed.2021.104693.
[42] M. Klarhöfer, B. Csapo, C. Balassy, J. C. Szeles, and E. Moser, “High-resolution blood flow velocity measurements in the human finger,” *Magn Reson Med*, vol. 45, no. 4, pp. 716–719, Apr. 2001, doi: 10.1002/mrm.1096.
[43] “Pressure and Blood Flow.” https://archive.math.arizona.edu/maw1999/blood/pressure.html (accessed Oct. 12, 2021).
[44] “Blood Flow In Arteries.” https://www.annualreviews.org/doi/epdf/10.1146/annurev.fluid.29.1.399 (accessed Jun. 23, 2022).
[45] E. Doutel, F. Galindo-Rosales, and L. Campo-Deaño, “Hemodynamics Challenges for the Navigation of Medical Microbots for the Treatment of CVDs,” *Materials*, vol. 14, p. 7402, Dec. 2021, doi: 10.3390/ma14237402.
[46] “Chapter 14.” https://kparker.bg-research.cc.ic.ac.uk/homepage/Mechanics%20of%20the%20Circulation/Chap_14/_Chapter_14.htm (accessed Jun. 23, 2022).
[47] E. P. W. Helps and D. A. McDonald, “Observations on laminar flow in veins,” *J Physiol*, vol. 124, no. 3, pp. 631–639, Jun. 1954.

[48] “Elastic Properties of Blood Vessels - Arteries and Veins - The Cardiovascular System - Medical Physiology, 3rd Edition.” https://doctorlib.info/physiology/medical/104.html (accessed Oct. 19, 2021).
[49] “18.5C: Venous Blood Pressure,” *Medicine LibreTexts*, Jul. 21, 2018. https://med.libretexts.org/Bookshelves/Anatomy_and_Physiology/Book%3A_Anatomy_and_Physiology_(Boundless)/18%3A_Cardiovascular_System%3A_Blood_Vessels/18.5%3A_Systemic_Blood_Pressure/18.5C%3A_Venous_Blood_Pressure (accessed Sep. 12, 2021).
[50] E. M. Gofur and B. Bordoni, “Anatomy, Head and Neck, Cerebral Blood Flow,” in *StatPearls*, Treasure Island (FL): StatPearls Publishing, 2021. Accessed: Sep. 07, 2021. [Online]. Available: http://www.ncbi.nlm.nih.gov/books/NBK538134/
[51] M. Heil, “Department of Mathematics, University of Manchester, Oxford Road, Manchester M13 9PL, UK,” p. 45.
[52] K. Larson, “Can You Estimate Modulus From Durometer Hardness for Silicones? Yes, but only roughly … and you must choose your modulus carefully!,” Sep. 2017.
[53] A. H. Ullah, “Advanced Measurements and Analyses of Flow Past Three-Cylinder Rotating System,” 2020, Accessed: May 25, 2022. [Online]. Available: https://library.ndsu.edu/ir/handle/10365/31833
[54] “Durometer Shore Hardness Scale,” *Smooth-On, Inc.* https://www.smooth-on.com/page/durometer-shore-hardness-scale/ (accessed Oct. 21, 2021).
[55] A. N. Gent, “On the Relation between Indentation Hardness and Young’s Modulus,” *Rubber Chemistry and Technology*, vol. 31, no. 4, pp. 896–906, Sep. 1958, doi: 10.5254/1.3542351.

APPENDIX A. YOUNG'S MODULUS APPROXIMATION FROM SHORE HARDNESS

Theory/Background

Young's modulus is a commonly used material property generally obtained from the stress and strain curve of a tension test. However, this type of testing requires the material sample to be tested to be of a minimum size and thickness. If the material sample available isn't compatible with the tension testing requirements, it is possible to approximate the Young's modulus from Shore hardness testing.

Shore hardness uses an indenter to determine the hardness of the material based on several scales. Shore A is for flexible molded rubbers of varying in hardness from very flexible and soft to hard with limited flexibility. At the high end of the spectrum, semi-rigid plastics can be measured using the Shore A scale. Another common scale is Shore D which is for semi-rigid plastics, hard rubbers, and hard plastics [54].

In 1958, A. N. Gent proposed the most well-known correlation between Young's modulus and hardness. It relates Young's modulus in megapascals to the measured Shore A hardness, provided the hardness is between 80A and 20A.

$$E = \frac{0.0981(56+7.62336S)}{0.137505(254-2.54S)}, \tag{A.1}$$

In the above equation, E is the Young's modulus and S is the Shore A hardness [55]. Other approximations have been suggested for Shore A and Shore D hardness scales.

Additional correlations between Young's modulus and Shore hardness include Ruess's approximation,

$$\log_{10} E = 0.0235S - 0.6403 \tag{A.2}$$

where E is the Young's modulus in MPa and S is the Shore A hardness. Ruess's equivalent correlation for Shore D hardness scale is

$$\log_{10} E = 0.0235(S + 50) - 0.6403. \quad \text{(A.3)}$$

Qi estimated the relationship between ASTM D2240 type D hardness and Young's modulus for a conical indenter with a 15° cone to be

$$S_D = 100 - \frac{20(-78.188 + \sqrt{6113.36 + 781.88E}}{E} \quad \text{(A.4)}$$

where S_D is the type D hardness and E is in MPa [52].

Methods

To get the Shore hardness of a material, a durometer is needed. NDSU has three options for Shore A durometers and one Shore D durometer. The durometers are in the Materials Testing Lab (Room 127) in Dolve Hall. Two of the Shore A durometers available are shown in Figure A1.

Figure A1. Two Shore A hardness durometers.

The blue and silver, pen-like durometer on the left gives a 5-value range of the hardness from 0 to 100. The black and silver, circular top Rex durometer on the right gives a singular value of hardness per reading up to the hundredths. The first durometer is better for a quick check of the hardness without much accuracy, while the second is better for determining the hardness to be used to determine other properties.

The Rex durometer has an operating manual for additional information. One keynote is that specimens should be at least ¼" thick. If the material sample is not ¼" thick, samples can be stacked to obtain the required thickness.

Because rubber, silicone, and plastics tend to have varying properties throughout the sample, be prepared to take multiple readings and average them to find the material's hardness. To take readings, turn on the durometer (if applicable, otherwise make sure the red button at the top is completely compressed) and press firmly into the sample. Applying too much force may

cause the hardness of the material below the sample to be read. Applying insufficient force will lead to inaccurate readings as well. There are material samples of known hardness available to determine the necessary force to take readings.

After averaging the readings, apply equation (A.1) to find the Young's modulus of the material based on its Shore A hardness.

APPENDIX B. MATLAB CODE FOR DETERMINING OSCILLATION FREQUENCY

The following Matlab code was used to determine the oscillation frequency of self-excited oscillations. This requires the collected data to be in Excel file of 4 columns – starting with time and ending with the downstream pressure readings. Though the FFT is calculated for all of the pressure columns, the code only plots and determines the maximum frequency for the downstream pressure vales.

Matlab Code:

```
%import the required oscillation pressure data; name the table appropriately, this one is named
%'A'
%table A does not include headings. col1=time, col2=p1, col3=p2, col4=p4
clc; %clears command window without getting rid of variables in workspace
%separating time and pressures
t = A{:,1};
p1 = A{:,2}; p2 = A{:,3}; p4 = A{:,4};
%fft of pressures
y1 = fft(p1); y2 = fft(p2); y4 = fft(p4);
%abs values of ffts
x1 = abs(y1); x2 = abs(y2); x4 = abs(y4);
%create frequency vector
b = 1:1:75000; B = transpose(b);
freq = B./15;
%plotting
%get rid of first number. plot (2:102,:) to get graph of peaks.
P1 = x1(2:75000,:); P2 = x2(2:75000,:);
P4all = x4(2:75000,:); Fall = freq(2:75000,:);
P4some = x4(2:102,:); Fsome = freq(2:102,:);
plot(Fsome,P4some)
%finding max values, change Freq number (21) once max of P4 is known from I.
format long; format compact
[M,I] = max(P4all)
Freq = Fall(21,:)
```